

THE PHYSICAL PROPERTIES OF *FERMI*-4LAC FLAT SPECTRUM RADIO QUASARS

CAN TAN¹, RUI XUE^{2, 3, 4}, LEI-MING DU¹, SHAO-QIANG XI^{2, 3}, ZE-RUI WANG^{2, 3, 5}, AND ZHAO-HUA XIE¹

May 20, 2020

ABSTRACT

In this work, we collect quasi-simultaneous infrared, optical, X-ray and γ -ray data of 60 *Fermi*-4LAC flat spectrum radio quasars (FSRQs). In the framework of the conventional one-zone leptonic model, we investigate the physical properties of *Fermi*-4LAC FSRQs' jets by modeling their quasi-simultaneous spectral energy distributions (SEDs). Our main results are summarized as follows. (1) There is a linear correlation between synchrotron peak frequency and curvature of the electron energy distribution. As suggested by previous works, the slope of the best linear fitting equation of this correlation is consistent with statistic acceleration which needs a fluctuation of fractional acceleration gain. (2) The gamma-ray dissipation regions are located at the range from 0.1 to 10 pc away from the super-massive black hole, and located outside the broad-line region (BLR) and within the dusty torus (DT). (3) A size relation P_e (the kinetic power carried in relativistic electrons) $\sim P_B$ (Poynting flux) $\leq P_r$ (the radiative power) $< P_p$ (the kinetic power in cold protons) is found in our modeling. Among them, $P_e \sim P_B$ suggests that SEDs of almost all FSRQs with parameters are close to equipartition between the magnetic field and the relativistic electrons. The $P_e < P_r$ suggest that the most energy of the relativistic electrons are dissipated by EC radiation for FSRQs. (4) There is an anti-correlation between the peak energy of SEDs (γ_{peak}) and the jet power (P_{jet}), which is consistent with the blazar sequence.

Keywords: radiation mechanisms: non-thermal–galaxies: jets–plasmas–quasars: general–flat spectrum radiation quasars: general

1. INTRODUCTION

Blazars are the most extreme and powerful subclass of active galactic nuclei (AGNs), and their observed emission is dominated by a relativistic jet pointed in the direction of the observer (Urry, & Padovani 1995). They have high luminosity, large amplitude and rapid variability, high and variable polarization, radio core dominance, and apparent super-luminal speeds (Urry, & Padovani 1995; Massaro et al. 2015). Blazars are divided into BL Lacertae objects (BL Lacs) with weak or no emission lines ($EW < 5\text{\AA}$) and flat spectrum radio quasars (FSRQs) with stronger emission lines $EW \geq 5\text{\AA}$ (Urry, & Padovani 1995). The spectral energy distribution (SED) of blazars are characterized by two bumps in the $\log\nu - \log\nu F_\nu$ diagram. The low energy bump at the IR-optical-UV band is well explained by synchrotron emission from relativistic electrons, and the high energy bump at the GeV-TeV gamma-ray band is attributed to the inverse Compton (IC) scattering (e.g., Dermer 1995; Dermer, & Schlickeiser 2002; Böttcher 2007). The seed photons for IC process could be from the synchrotron radiation (synchrotron self-Compton, SSC; (e.g., Maraschi et al. 1992; Tavecchio et al. 1998) or from external photon fields (external-Compton, EC), such as the accretion disk (e.g., Dermer, & Schlickeiser 1993), the broad-line

region (BLR; e.g., Sikora et al. 1994; Fan et al. 2006), and the dusty torus (DT; e.g., Błażejowski et al. 2000; Arbeiter et al. 2002; Sokolov, & Marscher 2005). Also, the hadronic model is an alternative explanation for the high-energy emission (e.g., Mannheim 1993; Mücke et al. 2003; Dermer et al. 2012; Dimitrakoudis et al. 2012; Xue et al. 2019). The modeling of SEDs allows us to investigate the intrinsic physical properties of emitting region in the jet (e.g., Ghisellini, & Tavecchio 2008, 2009, 2010; Zhang et al. 2014; Yan et al. 2014; Ding et al. 2017; Chen 2018).

Landau et al. (1986) find an anti-correlation between synchrotron peak frequency and its curvature. This correlation can be explained in terms of the acceleration processes of electrons (Massaro et al. 2004; Tramacere et al. 2011). Rani et al. (2011) and Ding et al. (2017) check this correlation by modeling the SEDs. Based on previous studies (Massaro et al. 2004; Tramacere et al. 2011), Chen (2014) deduce the theoretical relationship between synchrotron peak frequency and its curvature for different acceleration mechanisms. For stochastic acceleration, statistical acceleration with energy-dependent acceleration, and fractional acceleration gain, the predicted theoretical value of slope k ($1/b_{\text{syn}} = k \log\nu_p + m$, where b_{syn} is the synchrotron curvature, $\log\nu_p$ is the logarithm of the synchrotron peak frequency) is 2, 5/2, and 10/3, respectively. The result of Chen (2014) is $k = 2.04 \pm 0.03$, which favors stochastic acceleration mechanism. Xue et al. (2016) collected a large sample of BL Lacs and FSRQs. The slope of BL Lacs ($k = 1.87 \pm 0.19$) is consistent with the result of Chen (2014). On the other hand, the slope of FSRQs ($k = 3.69 \pm 0.24$) is closely consistent with the statistic acceleration for the case of fluctuation of fractional acceleration gain Chen (2014).

¹ Department of Physics, Yunnan Normal University, 650500, Kunming, China

² School of Astronomy and Space Science, Nanjing University, 210093, Nanjing, China

³ Key laboratory of Modern Astronomy and Astrophysics (Nanjing University), Ministry of Education, Nanjing 210023, People's Republic of China

⁴ Corresponding author, email: dg1726013@smail.nju.edu.cn

⁵ Corresponding author, email: zerui.wang62@163.com

The location of the dissipation regions, where the bulk energy of the jet is converted to a distribution of highly relativistic particles, can be a clue to understand the origin of ambient photon fields in the jets (e.g., Agudo et al. 2011; Dotson et al. 2012; Nalewajko et al. 2014; Böttcher, & Els 2016). However, there is no consensus on the location of the dissipation region. Poutanen, & Stern (2010) shows that the sharpness and position of γ -ray breaks can be reproduced by the absorption via photon-photon pair production on HeII Lyman recombination continuum and lines. Their result implies that the location of the emission region is close to the super-massive black hole (SMBH). On the other hand, the new γ -ray data from *Fermi*-LAT and the currently operational Cerenkov telescopes indicate that the dissipation region is actually quite remote from SMBH (e.g., Madejski, & Sikora 2016). There are two main diagnostics for the energy dissipation region: (i) the variability timescales (e.g., Abdo et al. 2010; Jorstad et al. 2010; Tavecchio et al. 2010; Liu et al. 2011; Agudo et al. 2012; Grandi et al. 2012; Brown 2013; Ramakrishnan et al. 2015), and (ii) fitting the SEDs (e.g., Dermer et al. 2009; Ghisellini, & Tavecchio 2009; Georganopoulos et al. 2012; Zdziarski et al. 2012; Kang et al. 2014; Zheng et al. 2017; Yan et al. 2018). Since the variability timescale only implies the size of dissipation region but not at any particular location, we consider the SED argument to study the location of dissipation region in this work (e.g., Pacciani et al. 2014; Yan et al. 2015; Wu et al. 2018).

The *Fermi*-4LAC source catalogue was released recently (The *Fermi*-LAT collaboration 2019). With the new gamma-ray data, we fit the SEDs of 60 *Fermi*-4LAC FSRQs which have contemporaneous multi-wavelength observation data to analyze the properties of the jets, trace the location of the dissipation regions, and explore the particle acceleration mechanisms in the framework of the conventional leptonic EC model. This paper is organized as follows: In Sect. 2, we present the sample, the model description is presented in Sect. 3. Then, results and discussions are shown in Sect. 4. Finally, we end with a conclusion of this work in Sect. 5. The cosmological parameters $H_0 = 70 \text{ km s}^{-1} \text{ Mpc}^{-1}$, $\Omega_0 = 0.3$, and $\Omega_\Lambda = 0.7$ are adopted in this work.

2. THE SAMPLE

We collect a sample with 60 FSRQs from the forth LAT AGN catalogue (4LAC). Their broadband SEDs from infrared to γ -ray band are available based on (quasi-) simultaneous observations. Since the radio data cannot be explained by one-zone leptonic model and most of them on the SED Builder are collected around the 1990s, we do not consider the radio data. First, we obtain all data and corresponding observation times in the SSDC SED Builder, an online service developed at the Space Science Data Center (Stratta et al. 2011)⁶. Second, we search for the intersection of observation time from infrared to X-ray band, and ensure that the interval of observation time between any two bands shall not exceed 7 days. We obtain the *Fermi* GeV data by integrating 2 months⁷ that include the previous time intersection, because the gamma-ray data on the SSDC website are

⁶ <http://tools.ssdsc.asi.it/SED/>

⁷ see Appendix A for more details

all collected by annual integration and this website has not yet collected the data of *Fermi*-4LAC. Finally, we collect the quasi-simultaneous data from infrared to γ -ray band. The data from infrared to X-ray band are observed within one week, and the *Fermi*-LAT data are integrated two months. Therefore, the multi-frequency data in our sample are quasi-simultaneous, but not really simultaneous.

Details are presented in Table 1, where column(1) gives the name of the Fermi catalogue, column(2) gives the source name, column(3) gives the right ascension, column(4) gives the declination, column (5) gives the observation time between infrared and X-ray band, and column(6) gives the integration time of γ -ray.

For the broad-line luminosity of 44 FSRQs in our sample, we select these values from Ghisellini, & Tavecchio (2009) and Xue et al. (2016). For FSRQs without a measured broad-line luminosity, we use the mean value of $10^{44.87} \text{ erg s}^{-1}$ in our sample.

3. THE MODEL DESCRIPTION

In this section, all quantities are measured in the co-moving frame, unless specified otherwise. We adopt the conventional one-zone EC model to fit the SEDs, which is widely used to study the properties of blazars (e.g., Ghisellini et al. 2010; Shah et al. 2017; Arsioli, & Chang 2018). The dissipation region is assumed to originate from a single spherical region with radius R , which is composed of a plasma of relativistic electrons and cold protons in a uniformly entangled magnetic field B . Because of the beaming effect, the observed radiation is strongly boosted by a relativistic Doppler factor δ ⁸. In the framework of leptonic model, since the log-parabolic electron spectrum is helpful for the study of acceleration mechanisms, we assume that the steady-state electron energy distribution is a log-parabolic spectrum (e.g., Kardashev 1962; Massaro et al. 2004, 2006; Paggi et al. 2009; Tramacere et al. 2011; Lan et al. 2019),

$$N(\gamma) = N \left(\frac{\gamma}{\gamma_0} \right)^{-s-r \log(\frac{\gamma}{\gamma_0})}, \quad \gamma_{\min} \leq \gamma \leq \gamma_{\max}, \quad (1)$$

where N is the normalization constant in units of $1/\text{cm}^3$, γ is the the electron Lorentz factor, γ_0 is the reference energy. s is the spectral index, r is the spectral curvature, γ_{\min} and γ_{\max} are the minimum and maximum electron Lorentz factors.

After assuming a steady-state electron distribution $N(\gamma)$, we can calculate the synchrotron, SSC and EC emissions from jets. The synchrotron emission coefficients is calculated with

$$j_{\text{syn}}(\nu) = \frac{1}{4\pi} \int N(\gamma) P(\nu, \gamma) d\gamma, \quad (2)$$

where ν is the frequency, $P(\nu, \gamma)$ is the mean emission coefficient for a single electron integrated over the isotropic distribution of pitch angles (e.g., Ghisellini et al. 1988; Katarzyński et al. 2001). And the synchrotron absorption coefficient is calculated with

$$\alpha_{\text{syn}}(\nu) = -\frac{1}{8\pi\nu^2 m_e} \int d\gamma P(\nu, \gamma) \gamma^2 \frac{\partial}{\partial \gamma} \left[\frac{N(\gamma)}{\gamma^2} \right]. \quad (3)$$

⁸ For the relativistic jet close to the line of sight in blazars with a viewing angle of $\theta \lesssim 1/\Gamma$, we have $\delta = [\Gamma(1 - \beta \cos\theta)]^{-1} \approx \Gamma$.

Then we can calculate the synchrotron intensity using the radiative transfer equation

$$I_{\text{syn}}(\nu) = \frac{j_{\text{syn}}(\nu)}{\alpha_{\text{syn}}(\nu)} \left[1 - \frac{2}{\tau(\nu)^2} (1 - \tau e^{-\tau(\nu)} - e^{-\tau(\nu)}) \right], \quad (4)$$

where $\tau(\nu) = \alpha_{\text{syn}}(\nu)2R$ is the optical depth.

The SSC and EC emission coefficients are given as

$$j_{\text{IC}} = \frac{h\epsilon}{4\pi} \int d\epsilon_0 n(\epsilon_0) \int \gamma N(\gamma) C(\epsilon, \gamma, \epsilon_0), \quad (5)$$

where ϵ is the scattered photon energy in units of $m_e c^2$, ϵ_0 is the soft photon energy in units of $m_e c^2$, $n(\epsilon_0)$ is the number density of seed photons per energy interval and $C(\epsilon, \gamma, \epsilon_0)$ is the Compton kernel given by Jones (1968).

The only difference between EC process and SSC process is the origin of seed photons. For SSC process, the seed photons are the synchrotron photons emitted by the same population of electrons. Meanwhile, for EC process, the seed photons are considered to originate from BLR and DT (e.g., D'Ammando et al. 2016; Arsioli, & Chang 2018; Dotson 2018). We can calculate the energy density of BLR (μ_{BLR}) and DT (μ_{DT}) in the jet comoving frame according to (Hayashida et al. 2012)

$$\mu_{\text{BLR}} = \frac{\eta_{\text{BLR}} \Gamma^2 L_d}{3\pi x_{\text{BLR}}^2 c [1 + (x/x_{\text{BLR}})^3]} \quad (6)$$

and

$$\mu_{\text{DT}} = \frac{\eta_{\text{DT}} \Gamma^2 L_d}{3\pi x_{\text{DT}}^2 c [1 + (x/x_{\text{DT}})^4]}, \quad (7)$$

where $\eta_{\text{BLR}} = 0.1$ and $\eta_{\text{DT}} = 0.1$ are the fractions of the disk luminosity L_d reprocessed into BLR and DT radiation, respectively. x is the distance between the position of the dissipation region and the central black hole in the AGN frame. We assume that the characteristic distance of BLR is $x_{\text{BLR}} = 0.1 (L_d/10^{46} \text{ ergs}^{-1})^{1/2} \text{ pc}$ and the characteristic distance of DT is $x_{\text{DT}} = 2.5 (L_d/10^{46} \text{ ergs}^{-1})^{1/2} \text{ pc}$ (e.g., Ghisellini, & Tavecchio 2008). The radiation from both BLR and DT is taken as an isotropic blackbody with a peak at $2 \times 10^{15} \text{ Hz}$ (Tavecchio, & Ghisellini 2008) and $3 \times 10^{13} \text{ Hz}$ (Cleary et al. 2007), respectively.

Based on the above, we can calculate the IC intensity

$$I_{\text{IC}}(\nu) = j_{\text{IC}}(\nu)R, \quad (8)$$

since the medium is transparent for IC radiation. Finally, the total observed flux density can be calculated by

$$F_{\text{obs}}(\nu_{\text{obs}}) = \frac{\pi R^2 \delta^3 (1+z)}{D_L^2} (I_{\text{syn}}(\nu) + I_{\text{IC}}(\nu)), \quad (9)$$

where D_L is the luminosity distance, z is the redshift, and $\nu_{\text{obs}} = \nu \delta / (1+z)$, where ν is the frequency of photons in comoving frame. Since the very high energy (VHE) γ -ray photons will be absorbed by the extragalactic background light (EBL), we calculate the absorption in the GeV-TeV band by using the EBL model presented by Domínguez et al. (2011).

There are 11 free parameters in our model: R , B , δ , N , γ_0 , γ_{min} , γ_{max} , s , r , x , and L_d . Since most of these parameters cannot be directly observed and they are coupled to each other, it will take a long time to reproduce

the best SED if we allow all eleven parameters to be free. In this work, we adopt $\gamma_{\text{min}} = 48$ (Zhang et al. 2014) and $\gamma_{\text{max}} = 2 \times 10^6$ (Ghisellini et al. 2005), because our model is not sensitive to these two parameters. In addition, we estimate the disk luminosity through $L_d = 10 \times L_{\text{BLR}}$ as proposed by Ghisellini, & Tavecchio (2008).

Based on the above constraints, we can calculate the observed photon spectrum and the corresponding chi-square value χ^2 . These parameters are listed in Table 2, and its columns are as follows:

1. *Fermi* name;
2. Source name;
3. z , redshift;
4. $\log L_{\text{BLR}}$ (erg s^{-1}), logarithm of the broad-line luminosity;
5. R (10^{17} cm), the radius of the dissipation region;
6. B (G), the magnetic field;
7. δ , the Doppler factors;
8. s , the electron spectral index;
9. r , the curvature of the electron energy distribution;
10. N , the normalization of the electron energy distribution;
11. γ_0 (10^2), the reference energy;
12. x (pc), the distance between the dissipation region and SMBH;
13. χ^2 , $\chi^2 = \frac{1}{m-dof} \sum_{i=1}^m (\frac{\hat{y}_i - y_i}{\sigma_i})^2$, where m is the number of quasi-simultaneous observational data points, dof are the degrees of freedom, \hat{y}_i are the expected values from the model, y_i are the observed data and σ_i is the standard deviation for each data point. In our sample, these errors of data points from infrared to X-ray band are collected from the SSC website. For errors of data points can not be found, we take 1% of the observed infrared and optical flux and take 2% of the observed UV and X-ray flux as the errors of these data points (e.g., Aleksić et al. 2014).

We apply our model to fit the SEDs of 60 *Fermi* FS-RQs, and the fitting results are shown in Figure 1 – Figure 6. In these Figures, the radio data are shown in black circles, and the quasi-simultaneous data from infrared to gamma-ray band are shown in cyan circles. The green dashed line represents the synchrotron emission, the red dotted line represents the SSC emission, the purple and the yellow dashed line represent the EC emission, in which seed photons are from the BLR and DT, respectively, and the black solid curve is the total emission by summarizing of all the emission.

When assuming that the multi-wavelength emission is from one dissipation region, the required number density of relativistic electrons is so high that the synchrotron emission below the turnover frequency (normally $\nu < 10^{11} \text{ Hz}$) is inevitably self-absorbed. Previous studies

suggest that it would be more natural to explain the GHz radio data by the synchrotron emission produced from extended jet (e.g., [Ghisellini et al. 2009, 2010](#)). This work focuses on fitting the simultaneous broadband emission from inner jet, therefore we do not explain the radio data below the turnover frequency.

4. RESULTS AND DISCUSSION

4.1. The distributions

In Figure 7(a)–(f), we show the parameter distributions. The values of R are in the range of $(0.55 \sim 4.95) \times 10^{17}$ cm. The values of B are in the range of $0.11 \sim 0.62$ G, which is similar to [Ghisellini et al. \(1998\)](#), [Celotti, & Ghisellini \(2008\)](#), [Ghisellini et al. \(2011\)](#). The values of δ are in the range of $7 \sim 27$, which is consistent with [Ghisellini et al. \(1998\)](#) and observations ([Hovatta et al. 2009](#)). The range of s are from $1.57 \sim 2.4$, and the range of r are from $0.5 \sim 1.3$. We also show the distributions of the synchrotron peak frequency ν_s and the IC peak frequency ν_{IC} in Figure 7(g), the values of ν_s are in the range of $6.76 \times 10^{12} \sim 1.81 \times 10^{13}$ Hz and the values of ν_{IC} are in the range of $8.47 \times 10^{20} \sim 5.62 \times 10^{22}$ Hz. Our parameters are all within a reasonable range.

4.2. Particle acceleration mechanisms

There are two mechanisms, statistical and stochastic acceleration mechanisms, can produce the electron energy distribution that follows the log-parabolic law, resulting in a log-parabolic SED. In the framework of statistical acceleration which needs an energy-dependent acceleration probability, the electron energy distribution follows the log-parabolic law when acceleration efficiency is inversely proportional to their energy ([Massaro et al. 2004](#)). In this process, [Chen \(2014\)](#) suggested that the correlation between ν_p and b_{syn} is $\log \nu_p \approx 2/(5b_{\text{syn}}) + m$. While, in the framework of statistical acceleration which needs a fluctuations of fractional acceleration gain, the electron energy distribution follows the log-normal law when the energy gain fluctuations are a random variable around the systematic energy gain ([Tramacere et al. 2011](#)). In this process, ν_p and b_{syn} follow the correlation of $\log \nu_p \approx 3/(10b_{\text{syn}}) + m$ ([Chen 2014](#)). In the framework of stochastic acceleration, the log-parabolic distribution can be derived from a mono-energetic and instantaneous injection ([Tramacere et al. 2011](#)). In this process, [Chen \(2014\)](#) obtained the correlation of $\log \nu_p \approx 1/(2b_{\text{syn}}) + m$. Therefore, the theoretical expected values of slope are $10/3$, $5/2$ and 2 for the fractional acceleration gain fluctuation, energy-dependent acceleration probability and stochastic acceleration processes, respectively.

In order to study the particle acceleration of our sample, we plot the synchrotron peak frequency versus its curvature in Figure 8. In order to facilitate comparison with these theoretical values of [Chen \(2014\)](#), we use $1/b_{\text{syn}}$ ($b_{\text{syn}} = r/4$) to represent the synchrotron curvature. The Spearman test gives a significance level $p = 2.958 \times 10^{-4}$ and a coefficient of correlation $\rho = 0.464$. The bisector linear regression gives the best linear fitting equation as $1/b_{\text{syn}} = (3.22 \pm 0.52)\log \nu_p - (33.74 \pm 0.52)$, represented as a solid black line in Figure 8. The dashed red lines indicate the 1σ confidence bands. We find that the frequency of the synchrotron peak is moderately correlated to its curvature because of the following two rea-

sons. Firstly, it may be caused by the existence of different acceleration mechanisms for each FSRQ. Secondly, the synchrotron peak frequency ν_p is estimated by

$$\log \gamma_{\text{peak}} = \log \gamma_0 + (3 - s)/2r, \quad (10)$$

$$\nu_p = 3.7 \times 10^6 \gamma_{\text{peak}}^2 B \delta / (1 + z). \quad (11)$$

It can be seen that ν_p is derived by six free parameters that vary from source to source and all can contribute to the scatter of the $b_{\text{syn}} - \nu_p$ correlation. Therefore, it is natural to find that the significance of this correlation will be weakened. In spite of this, for our sample, the slope is $k = 3.22 \pm 0.52$, which is basically consistent with statistical acceleration in a fluctuation of fractional acceleration gain ([Chen 2014](#)).

[Chen \(2014\)](#) analyzed the correlation of ν_p and b_{syn} by fitting the broadband SEDs of 43 blazars with the second-degree polynomial function. He found the slope of $\log \nu_p - 1/b_{\text{syn}}$ relation was 2.04 ± 0.03 , and suggested that the stochastic acceleration mechanism is dominant in jet. However his sample is too small to separate them into FSRQs and BL Lacs. Moreover, FSRQs and BL Lacs are two different subclasses of AGN, so they may have different acceleration mechanisms. [Xue et al. \(2016\)](#) collected a much larger sample which is separated into FSRQs and BL Lacs, and found they show different correlation. For BL Lacs, the slope ($k = 1.87 \pm 0.19$) is consistent with the stochastic acceleration mechanism. For FSRQs, the slope ($k = 3.69 \pm 0.24$) is closely consistent with the statistical acceleration for the case of fluctuation of fractional acceleration gain. This particle acceleration mechanism of FSRQs is consistent with our modeling result. For some individual sources, [Kapanadze et al. \(2016, 2017, 2018\)](#) analysed the Swift-XRT observations of Mrk 421 in different periods, and found that the correlation of $E_p - b$ is weak or very weak. In addition, [Wang et al. \(2019\)](#) studied the $E_p - b$ relation of 14 BL Lac objects using the log-parabolic model ([Massaro et al. 2004](#)), and found no correlation between E_p and b . The possible reasons are as follows: (1) They used the Swift-XRT data points which are not enough to distribute a complete synchrotron peak spectrum, resulting in a different curvature values and no correlation between E_p and b . (2) For a single source (like Mrk 421 in [Kapanadze et al. 2016, 2017, 2018](#)), there may be several acceleration mechanisms (first-order Fermi acceleration, magnetic reconnection, shear acceleration, and stochastic acceleration etc.) and they compete with each other ([Kapanadze et al. 2018](#)), resulting in a weakness or even absence of E_p and b correlation. For a sample that contains more than tens objects, there will be a tendency for only one acceleration mechanism to dominate. For our sample, the dominant acceleration mechanism is statistical acceleration with a fractional acceleration gain.

4.3. Location of γ -ray emission region

The location of the γ -ray emitting region in blazars is still controversial. In general, the energy dissipation region is constrained by two diagnostics, which are finding the variability timescale (e.g., [Abdo et al. 2010](#); [Liu et al. 2011](#); [Grandi et al. 2012](#); [Brown 2013](#); [Ramakrishnan et al. 2015](#)) and fitting the SED (e.g., [Dermer et al. 2009](#); [Zdziarski et al. 2012](#); [Kang et al. 2014](#); [Zheng et](#)

al. 2017; Yan et al. 2018). In our work, we fit the quasi-simultaneous SEDs of 60 FSRQs with the one-zone leptonic model to constrain it. Here, we assume that the energy density of the external ambient fields are functions of the distance between the position of the dissipation region (x) and SMBH (see Equations. 6 and 7), where the x is determined by reproducing the γ -ray spectra. In Figure 9, we plot x as a function of the luminosity of an accretion disk (L_d) for our sample. It can be seen that the γ -ray dissipation regions in our modeling are located at the range from 0.1 to 10 pc, which means that most of them are located outside the BLR and within the DT. In the modeling, the soft photons for the EC radiation of 40 FSRQs are dominated by that from DT and the soft photons of other 20 FSRQs are dominated by that from BLR. Therefore, we find that the gamma-ray emission regions are located outside the BLR, and the soft photons for EC processes of most FSRQs are dominated by that of DT.

Our results are consistent with many previous works. For example, Fuhrmann et al. (2014) used the ‘time lag core shift’ method for quasar 3C 454.3 to estimate a lower limit for the distance of the bulk γ -ray production region and suggested that the gamma-ray emission region are ~ 0.8 -1.6 pc away from the SMBH. Jiang et al. (2018) used the lag times of PMN J2345-1555 to derive the optical and the γ -ray emitting regions coincide, which are located at $4.26^{+0.83}_{-0.79}$ pc away from 15 GHz core position in jet. In addition, if the gamma-ray dissipation regions are located inside BLR, the γ rays are likely to be absorbed through the $\gamma\gamma$ pair production. However, only 10% of blazars show a feature of attenuation in their γ -ray spectrum (Costamante et al. 2018). So, γ -ray should be produced in a region far from the SMBH. There are some different views. For example, Poutanen, & Stern (2010) fitted the SED of 3C 454.3 using the broken power-law distribution, and suggested that the γ -ray emission region lies inside the region of the BLR. However, the broken power-law distribution of the γ -ray spectrum of 3C 454.3 could arise equally well from a break in the electron energy distribution. In addition, Lei & Wang (2015) fitted the quasi-simultaneous SED of 4C +21.35 with a one-zone leptonic model. They suggested that the emitting regions locate within the BLR clouds and around the outer radius of the BLR during flaring states, while the emitting region locates beyond the DT, $x > x_{DT} \simeq 4.8$ pc, for quiescent state. Their results suggested that the location of the gamma-ray dissipation region is distinct in different states of source. Since the quasi-simultaneous data of our sample are in the steady state and the location of the emission regions are relatively diffuse for our sample, our results are more inclined to suggest that the dissipation zone is outside the BLR.

4.4. The physical properties of jet

The jet power P_{jet} is critical to understand the production and composition of the jets and we can estimate them through fitting the SED. We assume that the jet power is carried by relativistic electron, cold proton, magnetic field, and radiation, i.e.,

$$P_{\text{jet}} = \sum_i \pi R^2 \Gamma^2 c U_i, \quad (12)$$

where U_i ($i = e, p, B, r$) are the energy densities associated with the emitting electron U_e , cold proton U_p , magnetic field U_B , and radiation U_r measured in the comoving frame (Ghisellini et al. 2010), which are given by

$$U_e = m_e c^2 \int N(\gamma) \gamma d\gamma, \quad (13)$$

$$U_p = m_p c^2 \int N(\gamma) d\gamma, \quad (14)$$

$$U_B = B^2 / 8\pi, \quad (15)$$

$$U_r = \frac{L_{\text{obs}}}{4\pi R^2 c \delta^4}, \quad (16)$$

where L_{obs} is the total observed non-thermal luminosity, which is calculated from the model. Here, we assume that the charge neutrality is provided by one cold proton per relativistic electron (i.e. no electron-positron pairs). The calculated P_e , P_p , P_B , P_r , and P_{jet} are listed in Table 3.

In Figure 10, we plot P_e , P_p , P_B , and P_{jet} as a function of P_r . The relation $P_e \sim P_B \leq P_r < P_p$ can be found. The $P_e \sim P_B$ suggests that SEDs fitted with parameters that are close to the condition of equipartition between the magnetic field and the relativistic electrons, which is consistent with many previous studies, such as Böttcher et al. (2013). Both of P_e and P_B are in the range of $10^{44} - 10^{46} \text{ erg s}^{-1}$. For example, the P_e , P_B and P_p of 3C 279 and 3C 454.3 obtained also similar to those of Böttcher et al. (2013), indicating that the radiation processes and radiation efficiencies in the jet are similar even if they are modeled with different parameters and electron energy distributions. They also used the hadronic model to fit the SEDs of blazars. However, the characteristic break of two quasars of their sample cannot be well modeled at a few GeV energies, and the modeling required powers in relativistic protons are in the range $P_p \sim 10^{47} - 10^{49} \text{ erg s}^{-1}$, which exceed their Eddington luminosity. The $P_B \leq P_r$ implies that Poynting flux cannot account for the radiation power. It can be seen that $P_r/P_e \sim 0.5 - 4$, which indicates that a large fraction of the relativistic electron power would be used to produce the observed radiation. The result $P_e < P_r$ derived here suggest that the most energy of the relativistic electrons are dissipated by EC radiation.

There is an anti-correlation between γ_{peak} and P_{jet} in our sample, i.e., $P_{\text{jet}} = -2.58\gamma_{\text{peak}} + 54.695$ with $\rho = -0.625$ and $p = 9.26 \times 10^{-8}$ (in Figure 11), where $\log \gamma_{\text{peak}} = \log \gamma_0 + (3 - s)/2r$ is the peak energy of SED. This result is consistent with the prediction of the blazar sequence (Fossati et al. 1998; Ghisellini et al. 1998; Ghisellini, & Tavecchio 2008; Celotti, & Ghisellini 2008), which is usually explained as that the radiation cooling is stronger in powerful blazar. Qin et al. (2018) also found that the peak luminosity L_{peak} was inversely related to the peak frequency ν_{peak} and γ_{peak} to P_{jet} , both of which supported the blazar sequence. Although some works suggested that the sequence is the result of a selection effect (e.g., Padovani et al. 2003; Giommi et al. 2005), many works proposed that the blazar sequence is still theoretically valid (e.g., Ghisellini et al. 1998; Böttcher & Dermer 2002; Finke 2013).

5. CONCLUSIONS

On the basis of the systematic SED fitting with the one-zone leptonic model for the quasi-simultaneous SEDs of 60 *Fermi*-4LAC FSRQs, we investigate the jet physical properties of *Fermi*-4LAC FSRQs. Our main results are summarized below.

1. We find the correlation between the curvature $1/b_{\text{syn}}$ and peak frequency ν_p is $1/b_{\text{syn}} = (3.22 \pm 0.52)\log\nu_p - (33.74 \pm 0.52)$, and the slope $k = 3.22 \pm 0.52$ is consistent with statistical acceleration in a fluctuation of fractional acceleration gain. We suggest that statistical acceleration with a fractional acceleration gain is the dominant acceleration mechanism for FSRQs in the steady state SEDs .
2. The gamma-ray dissipation region is distinct in different states of source. We find that the γ -ray dissipation regions for most FSRQs in the steady state are located at the range from 0.1 to 10 pc during quiescent state, which mean that they are located

outside the BLR and within the DT.

3. We find a size relation $P_e \sim P_B \leq P_r < P_p$. The $P_e \sim P_B$ suggests that SEDs fitted with parameters are close to equipartition between the magnetic field and the relativistic electrons. The $P_e < P_r$ suggest that the most energy of the relativistic electrons are dissipated by EC radiation for FSRQs. Then, we find an anti-correlation between P_{jet} and γ_{peak} , which is consistent with the prediction of the blazar sequence.

We thank the anonymous referee for insightful comments and constructive suggestions. Part of this work is based on archival data, software or online services provided by the SPACE SCIENCE DATA CENTER (SSDC). This work is supported by the Joint Research Fund in Astronomy (Grant Nos 10978019, U1431123) under cooperative agreement between the National Natural Science Foundation of China (NSFC) and Chinese Academy of Sciences (CAS)and the Provincial Natural Science Foundation of Yunnan (Grant No 2019FB009).

APPENDIX

FERMI-LAT ANALYSIS

Fermi-LAT is a pair-production telescope with large effective area and large filed of view, covering in the energy band 20– > 300 GeV, which provides a full-sky coverage every 3 hr (Atwood et al. 2009). We used the SOURCE class events converting in both the front and back sections, but rejecting that above a zenith angle of 90° to reduce contamination by Earth limb emission. For each FSRQs, we selected the data collecting in the time interval (~ 2 months), in which observation from infrared to X-ray energy were performed simultaneously. Events extracted are within a 10° region of interest(ROI) centered at the position of each FSRQs and with energies in the range between 100 MeV and 100 GeV.

We employed the latest release *Fermi*-LAT Science Tool to determine the spectra in *Fermi*-LAT band. We derived the spectral points in 6 logarithmically spaced energy bins over 0.1-100 GeV for each target source. For each bin, we carried out an unbinned likelihood analysis modeling the target object as point sources with simple power-law photon spectra fixed index $\Gamma = 2$. The background model comprise the diffuse components(i.e., Galactic diffuse emission modeled by *gll_iem.v7.fits* and isotropic emission with spectrum shape by *iso_P8R3_SOURCE_V2.v01.txt*), and the Fourth Source Catalog sources (4FGL; Abdollahi et al. 2020) within each region of ROI enlarged by 5° excluding our target object. For each energy bin fitting, we always left the normalization of the diffuse components free and fixed the spectral parameters of background 4FGL source to catalog value. Upper limits on the flux at 95% confidence level were derived when the detection significance is lower than 2σ in a given bin.

REFERENCES

- Abdo, A. A., Ackermann, M., Ajello, M., et al. 2010, ApJ, 712, 957
- Abdollahi, S., Acero, F., Ackermann, M., et al. 2020, ApJS, 247, 33
- Agudo, I., Jorstad, S. G., Marscher, A. P., et al. 2012, Journal of Physics Conference Series, 012032
- Agudo, I., Jorstad, S. G., Marscher, A. P., et al. 2011, ApJL, 726, L13
- Aleksić, J., Ansoldi, S., Antonelli, L. A., et al. 2014, A&A, 567, A135
- Arbeiter, C., Pohl, M., & Schlickeiser, R. 2002, A&A, 386, 415
- Arsioli, B., & Chang, Y.-L. 2018, A&A, 616, A63
- Atwood, W. B., Abdo, A. A., Ackermann, M., et al. 2009, ApJ, 697, 1071
- Brown, A. M. 2013, MNRAS, 431, 824
- Böttcher, M. 2007, Ap&SS, 309, 95
- Böttcher, M., Reimer, A., Sweeney, K., et al. 2013, ApJ, 768, 54
- Böttcher, M., & Els, P. 2016, ApJ, 821, 102
- Błażejowski, M., Sikora, M., Moderski, R., et al. 2000, ApJ, 545, 107
- Böttcher, M., & Dermer, C. D. 2002, ApJ, 564, 86
- Celotti, A., & Ghisellini, G. 2008, MNRAS, 385, 283
- Chen, L. 2014, ApJ, 788, 179
- Chen, L. 2018, ApJS, 235, 39
- Costamante, L., Cutini, S., Tosti, G., et al. 2018, MNRAS, 477, 4749
- Cleary, K., Lawrence, C. R., Marshall, J. A., et al. 2007, ApJ, 660, 117
- D’Ammando, F., Orienti, M., Finke, J., et al. 2016, MNRAS, 463, 4469
- Dermer, C. D., & Schlickeiser, R. 1993, ApJ, 416, 458
- Dermer, C. D. 1995, ApJL, 446, L63
- Dermer, C. D., Murase, K., & Takami, H. 2012, ApJ, 755, 147
- Dermer, C. D., & Schlickeiser, R. 2002, ApJ, 575, 667
- Dermer, C. D., Finke, J. D., Krug, H., et al. 2009, ApJ, 692, 32
- Dimitrakoudis, S., Mastichiadis, A., Protheroe, R. J., et al. 2012, A&A, 546, A120
- Ding, N., Zhang, X., Xiong, D. R., et al. 2017, MNRAS, 464, 599
- Domínguez, A., Primack, J. R., Rosario, D. J., et al. 2011, MNRAS, 410, 2556
- Dotson, A., Georganopoulos, M., Kazanas, D., et al. 2012, ApJL, 758, L15
- Dotson, A. C. 2018, Ph.D. Thesis
- Fan, Z., Cao, X., & Gu, M. 2006, ApJ, 646, 8
- Fuhrmann, L., Larsson, S., Chiang, J., et al. 2014, MNRAS, 441, 1899
- Fossati, G., Maraschi, L., Celotti, A., et al. 1998, MNRAS, 299, 433
- Finke, J. D. 2013, ApJ, 763, 134

- Georganopoulos, M., Meyer, E. T., & Fossati, G. 2012, arXiv e-prints, arXiv:1202.6193
- Ghisellini, G., Celotti, A., Fossati, G., et al. 1998, *MNRAS*, 301, 451
- Ghisellini, G., Guilbert, P. W., & Svensson, R. 1988, *ApJL*, 334, L5
- Ghisellini, G., Tavecchio, F., & Chiaberge, M. 2005, *A&A*, 432, 401
- Ghisellini, G., & Tavecchio, F. 2008, *MNRAS*, 387, 1669
- Ghisellini, G., Tavecchio, F., & Ghirlanda, G. 2009, *MNRAS*, 399, 2041
- Ghisellini, G., & Tavecchio, F. 2010, *MNRAS*, 409, L79
- Ghisellini, G., Tavecchio, F., Foschini, L., et al. 2010, *MNRAS*, 402, 497
- Ghisellini, G., Tavecchio, F., Foschini, L., et al. 2011, *MNRAS*, 414, 2674
- Ghisellini, G., & Tavecchio, F. 2009, *MNRAS*, 397, 985
- Giommi, P., Piranomonte, S., Perri, M., et al. 2005, *A&A*, 434, 385
- Grandi, P., Torresi, E., & Stanghellini, C. 2012, *ApJL*, 751, L3
- Hayashida, M., Madejski, G. M., Nalewajko, K., et al. 2012, *ApJ*, 754, 114
- Hovatta, T., Valtaoja, E., Tornikoski, M., et al. 2009, *A&A*, 494, 527
- Jiang, Y.-G., Hu, S.-M., Chen, X., et al. 2018, arXiv e-prints, arXiv:1809.04984
- Jones, F. C. 1968, *Physical Review*, 167, 1159
- Jorstad, S. G., Marscher, A. P., Larionov, V. M., et al. 2010, *ApJ*, 715, 362
- Kang, S.-J., Chen, L., & Wu, Q. 2014, *ApJS*, 215, 5
- Kardashev, N. S. 1962, *Soviet Ast.*, 6, 317
- Katarzyński, K., Sol, H., & Kus, A. 2001, *A&A*, 367, 809
- Kapanadze, B., Dorner, D., Vercellone, S., et al. 2016, *ApJ*, 831, 102
- Kapanadze, B., Dorner, D., Romano, P., et al. 2017, *ApJ*, 848, 103
- Kapanadze, B., Vercellone, S., Romano, P., et al. 2018, *ApJ*, 858, 68
- Lan, M.-X., Xue, R., Xiong, D., et al. 2019, *ApJ*, 878, 140
- Landau, R., Golisch, B., Jones, T. J., et al. 1986, *ApJ*, 308, 78
- Lei, M., & Wang, J. 2015, *PASJ*, 67, 79
- Liu, H. T., Bai, J. M., Wang, J. M., et al. 2011, *MNRAS*, 418, 90
- Madejski, G. (Greg) ., & Sikora, M. 2016, *ARA&A*, 54, 725
- Mannheim, K. 1993, *A&A*, 269, 67
- Maraschi, L., Ghisellini, G., & Celotti, A. 1992, *ApJL*, 397, L5
- Massaro, E., Perri, M., Giommi, P., et al. 2004, *A&A*, 413, 489
- Massaro, E., Tramacere, A., Perri, M., et al. 2006, *A&A*, 448, 861
- Massaro, F., Thompson, D. J., & Ferrara, E. C. 2015, *A&A Rev.*, 24, 2
- Mücke, A., Protheroe, R. J., Engel, R., et al. 2003, *Astroparticle Physics*, 18, 593
- Nalewajko, K., Begelman, M. C., & Sikora, M. 2014, *ApJ*, 789, 161
- Pacciani, L., Tavecchio, F., Donnarumma, I., et al. 2014, *ApJ*, 790, 45
- Padovani, P., Perlmutter, E. S., Landt, H., et al. 2003, *ApJ*, 588, 128
- Paggi, A., Massaro, F., Vittorini, V., et al. 2009, *A&A*, 504, 821
- Poutanen, J., & Stern, B. 2010, *ApJL*, 717, L118
- Qin, L., Wang, J., Yang, C., et al. 2018, *PASJ*, 70, 5
- Ramakrishnan, V., Hovatta, T., Nieppola, E., et al. 2015, *MNRAS*, 452, 1280
- Rani, B., Gupta, A. C., Bachev, R., et al. 2011, *MNRAS*, 417, 1881
- Shah, Z., Sahayanathan, S., Mankuzhiyil, N., et al. 2017, *MNRAS*, 470, 3283
- Sikora, M., Begelman, M. C., & Rees, M. J. 1994, *ApJ*, 421, 153
- Sokolov, A., & Marscher, A. P. 2005, *ApJ*, 629, 52
- Stratta, G., Capalbi, M., Giommi, P., et al. 2011, arXiv e-prints, arXiv:1103.0749
- Tavecchio, F., & Ghisellini, G. 2008, *MNRAS*, 386, 945
- Tavecchio, F., Ghisellini, G., Bonnoli, G., et al. 2010, *MNRAS*, 405, L94
- Tavecchio, F., Maraschi, L., & Ghisellini, G. 1998, *ApJ*, 509, 608
- The Fermi-LAT collaboration 2019, arXiv e-prints, arXiv:1902.10045
- Tramacere, A., Massaro, E., & Taylor, A. M. 2011, *ApJ*, 739, 66
- Urry, C. M., & Padovani, P. 1995, *PASP*, 107, 803
- Wang, Y., Zhu, S., Xue, Y., et al. 2019, *ApJ*, 885, 8
- Wu, L., Wu, Q., Yan, D., et al. 2018, *ApJ*, 852, 45
- Xue, R., Luo, D., Du, L. M., et al. 2016, *MNRAS*, 463, 3038
- Xue, R., Liu, R.-Y., Petropoulou, M., et al. 2019, *ApJ*, 886, 23
- Yan, D., Zeng, H., & Zhang, L. 2014, *MNRAS*, 439, 2933
- Yan, D., Wu, Q., Fan, X., et al. 2018, *ApJ*, 859, 168
- Yan, D., Zhang, L., & Zhang, S.-N. 2015, *MNRAS*, 454, 1310
- Zdziarski, A. A., Sikora, M., Dubus, G., et al. 2012, *MNRAS*, 421, 2956
- Zhang, J., Sun, X.-N., Liang, E.-W., et al. 2014, *ApJ*, 788, 104
- Zheng, Y. G., Yang, C. Y., Zhang, L., et al. 2017, *ApJS*, 228, 1

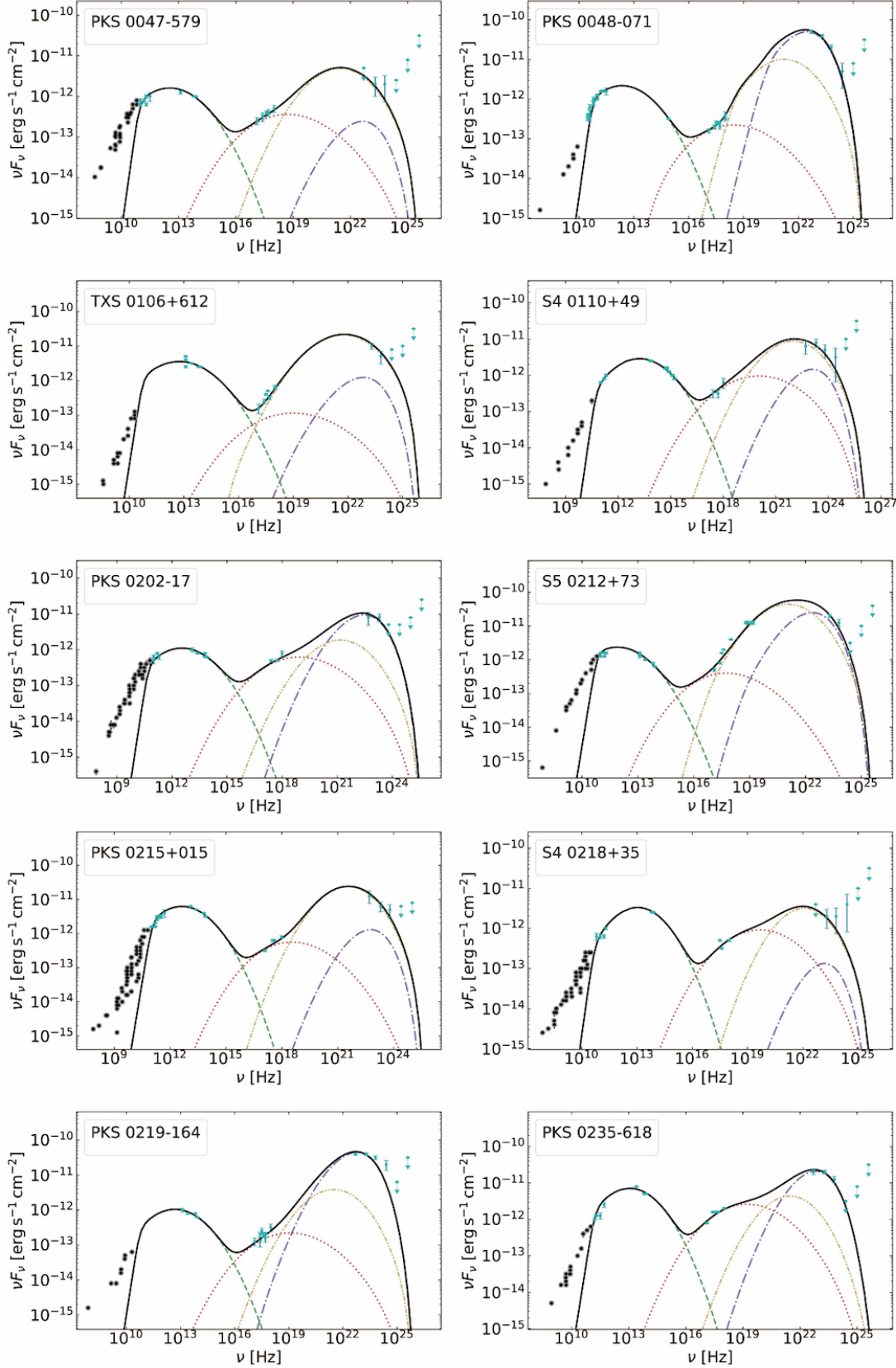


Figure 1. Comparisons of predicted multi-wavelength spectra with observed data for PKS 0047-579, PKS 0048-071, TXS 0106+612, S4 0110+49, PKS 0202-17, S5 0212+73, PKS 0215+015, S4 0218+35, PKS 0219-164, and PKS 0235-618, respectively. The radio data are shown in gray, and the quasi-simultaneous data from infrared to gamma-ray band are shown in blue. The green dashed line represents the synchrotron emission, the red dotted line represents the SSC emission, the purple dashed line and the yellow dashed line represents the EC emission, which seed photons from the BLR and DT, respectively, and the black solid curve is the total emission by summation of all the emission components.

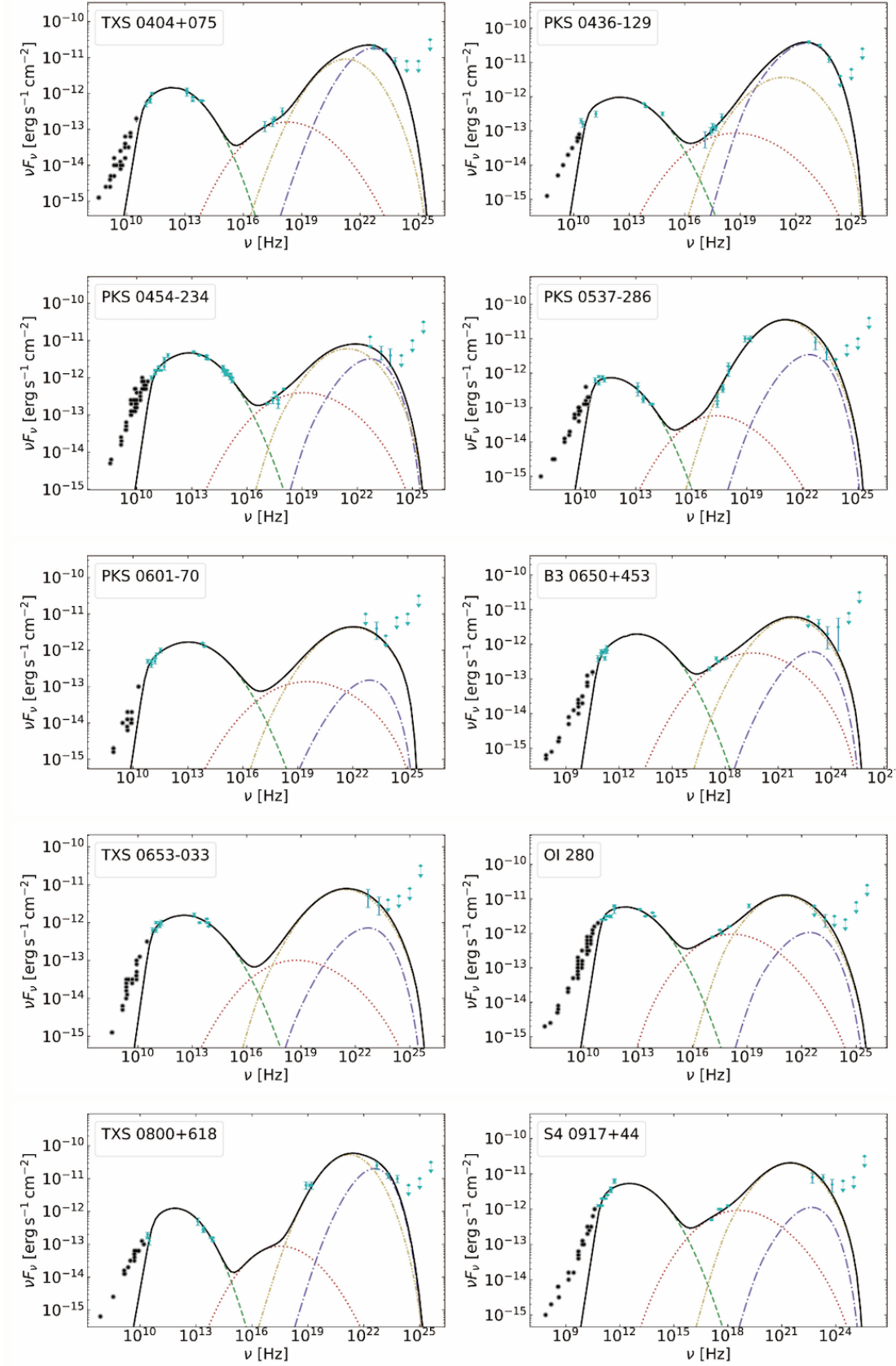


Figure 2. Comparisons of predicted multi-wavelength spectra with observed data for TXS 0404+075, PKS 0436-129, PKS 0454-234, PKS 0537-286, PKS 0601-70, B3 0650+453, TXS 0653-033, OI 280, TXS 0800+618, and S4 0917+44, respectively. The symbols and lines are the same as shown in Figure 1.

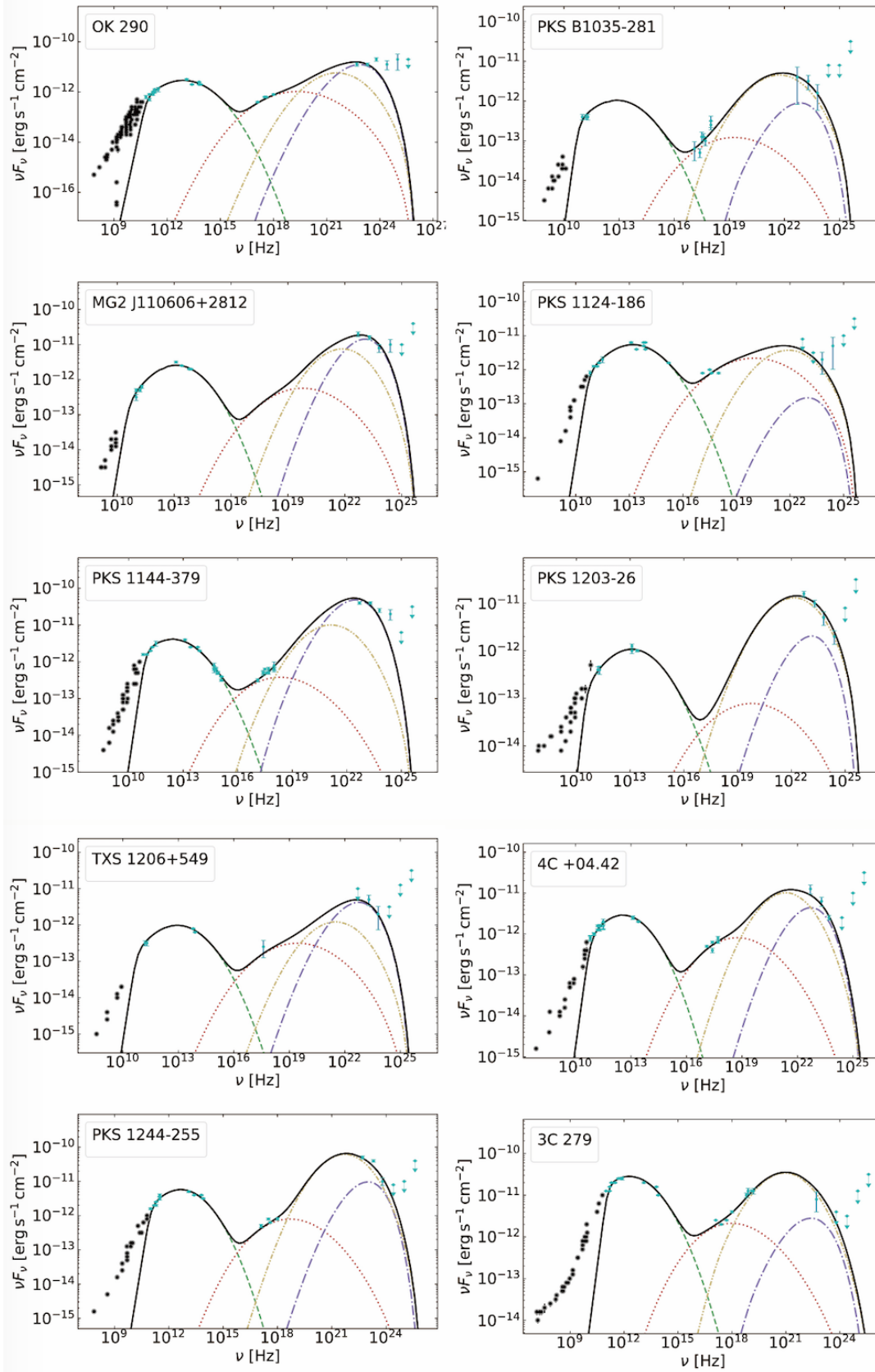


Figure 3. Comparisons of predicted multi-wavelength spectra with observed data for OK 290, PKS B1035-281, MG2 J110606+2812, PKS 1124-186, PKS 1144-379, PKS 1203-26, TXS 1206+549, 4C +04.42, PKS 1244-255, 3C 279, respectively. The symbols and lines are the same as shown in Figure 1.

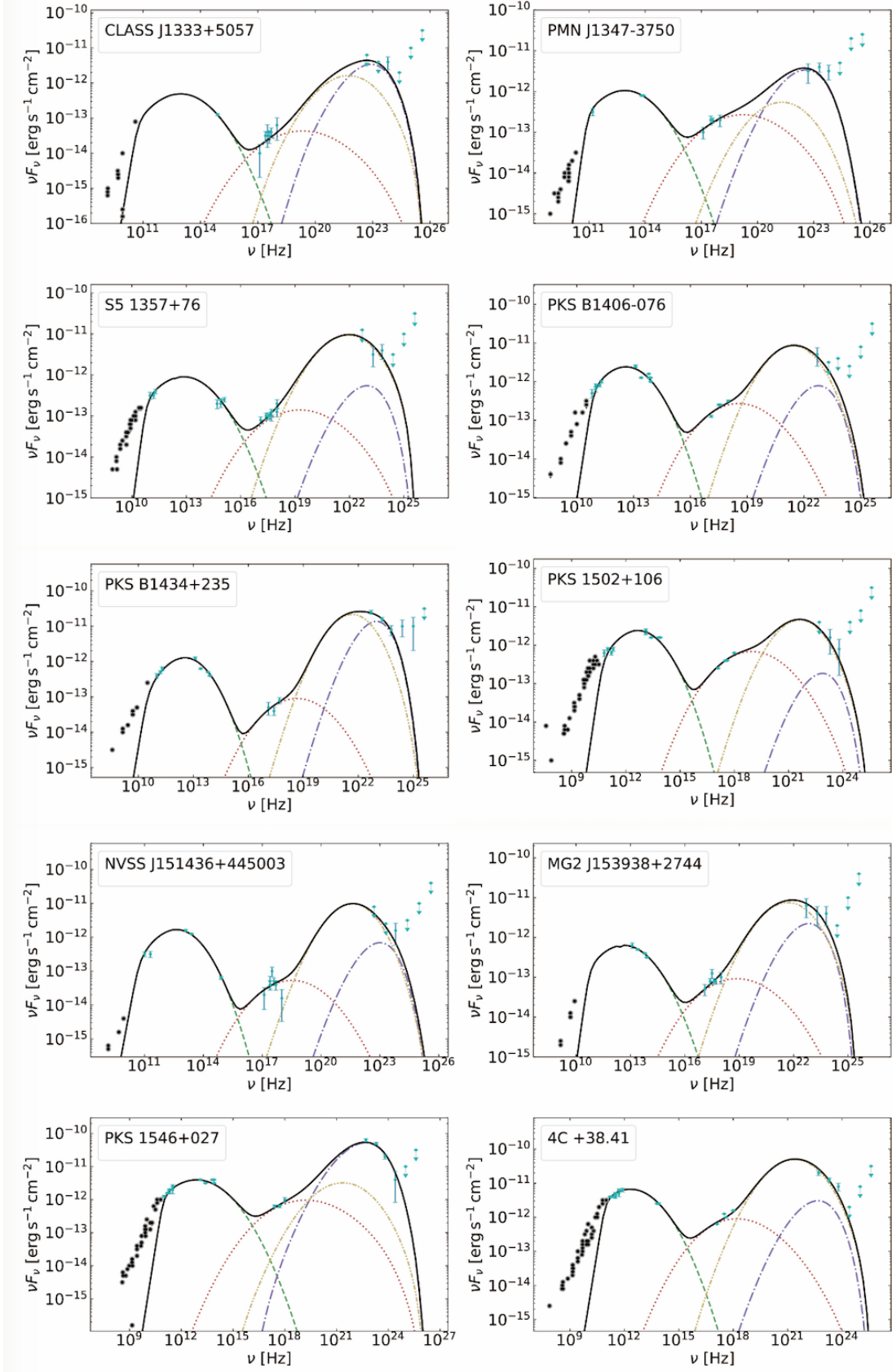


Figure 4. Comparisons of predicted multi-wavelength spectra with observed data for CLASS J1333+5057, PMN J1347-3750, S5 1357+76, PKS B1406-076, PKS B1434+235, PKS 1502+106, NVSS J151436+445003, MG2 J153938+2744, PKS 1546+027, 4C +38.41, respectively. The symbols and lines are the same as shown in Figure 1.

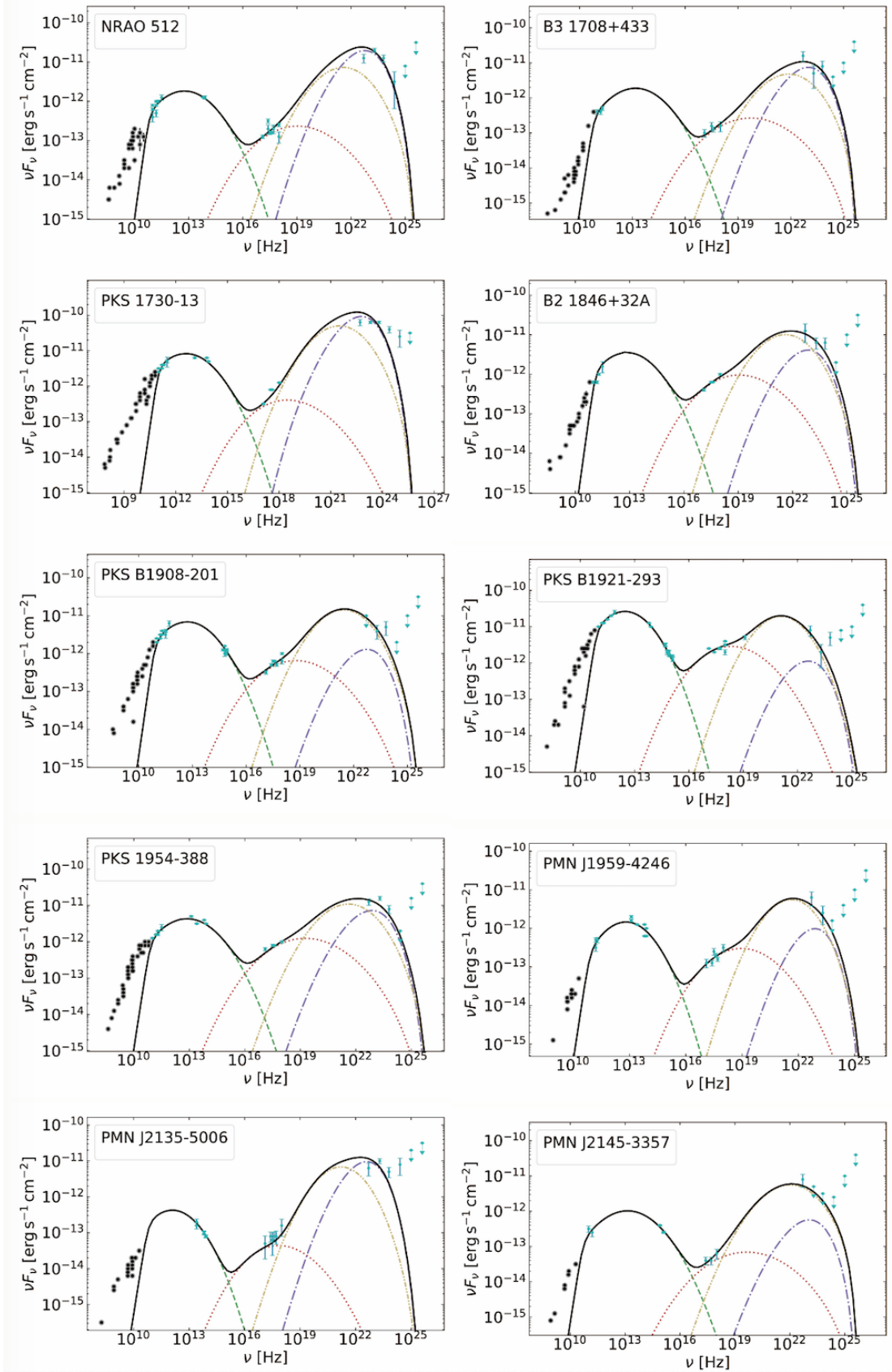


Figure 5. Comparisons of predicted multi-wavelength spectra with observed data for NRAO 512, B3 1708+433, PKS 1730-13, B2 1846+32A, PKS B1908-201, PKS B1921-293, PKS 1954-388, PMN J1959-4246, PMN J2135-5006, PMN J2145-3357, respectively. The symbols and lines are the same as shown in Figure 1.

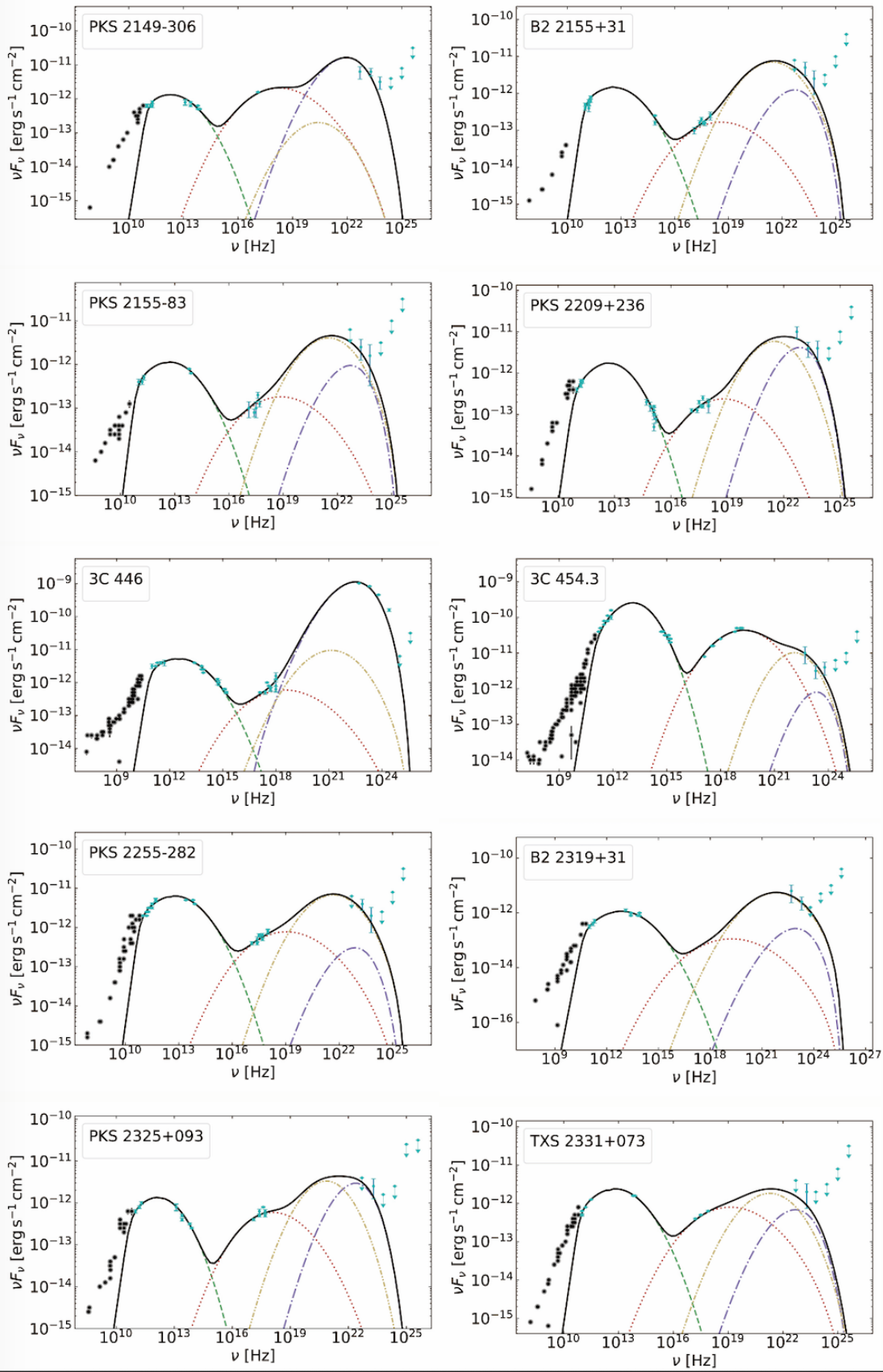


Figure 6. Comparisons of predicted multi-wavelength spectra with observed data for PKS 2149-306, B2 2155+31, PKS 2155-83, PKS 2209+236, 3C 446, 3C 454.3, PKS 2255-282, B2 2319+31, PKS 2325+093, TXS 2331+073, respectively. The symbols and lines are the same as shown in Figure 1.

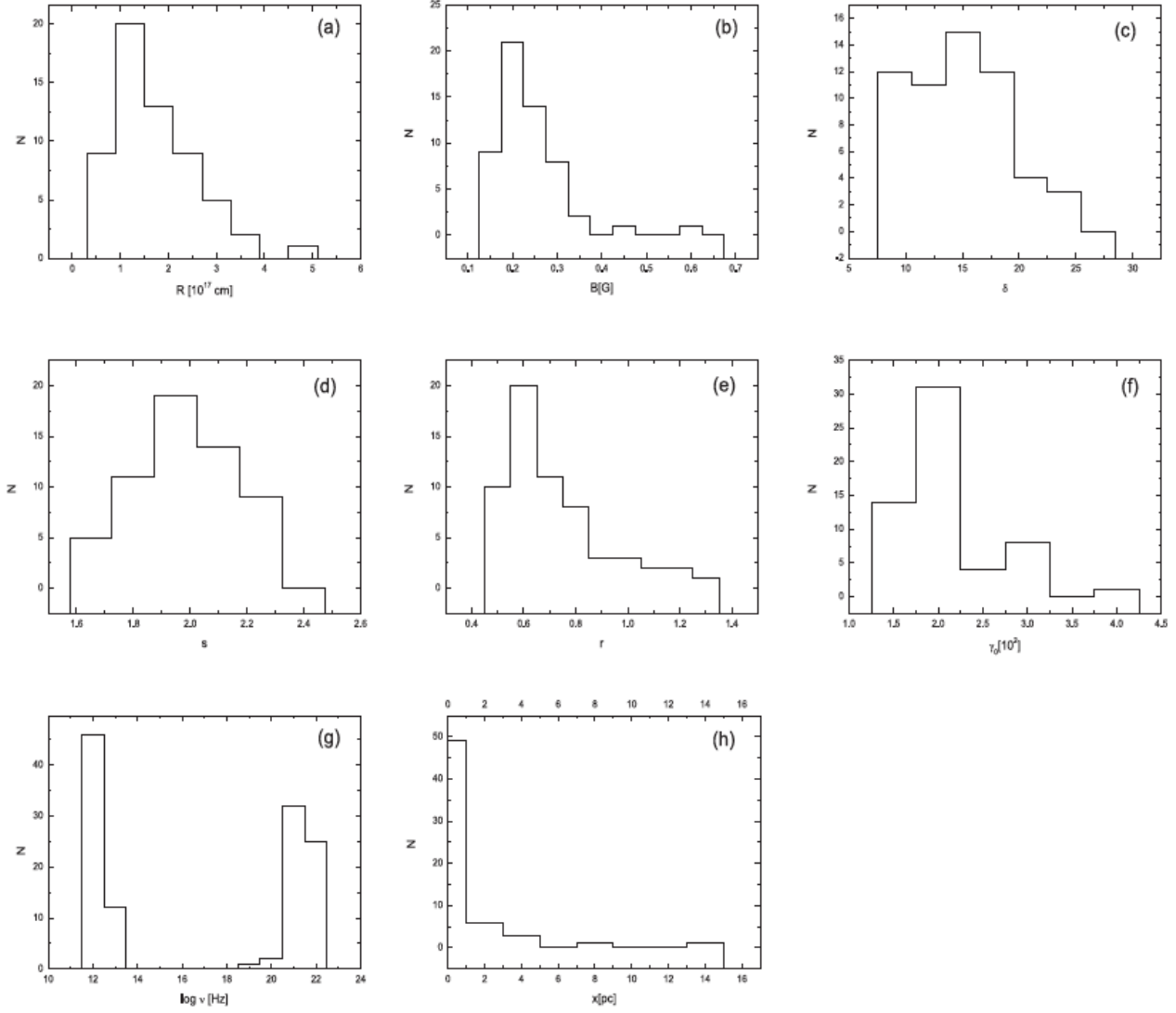


Figure 7. Distribution of the radiation region R (a), the magnetic field B (b), the Doppler factors δ (c), the spectral index s (d), the spectral curvature r (e), the reference energy γ_0 (f), the two peak frequencies ν_{syn} and ν_{IC} (h), and the distance x (h) between the dissipation region and the central black hole.

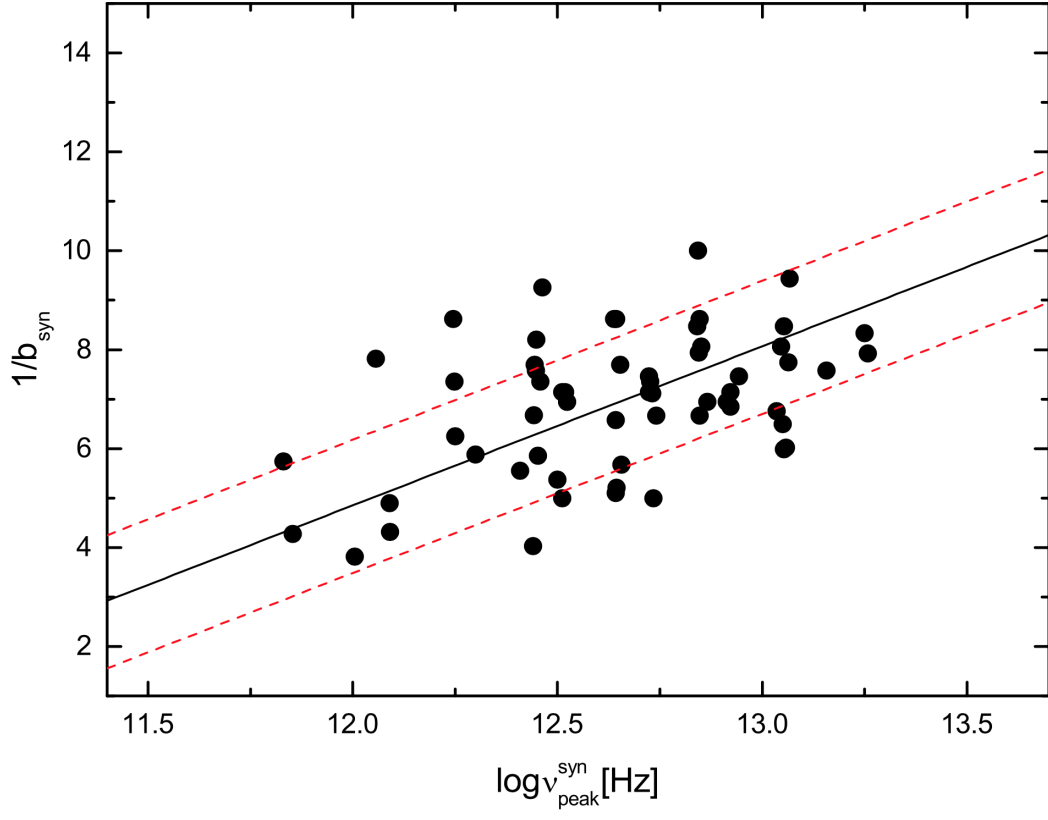


Figure 8. The synchrotron peak frequency versus synchrotron curvature (in $1/b_{\text{syn}}$). The solid line is the best linear fit ($p = 2.958 \times 10^{-4}$) and the dashed red lines indicate 1σ confidence bands.

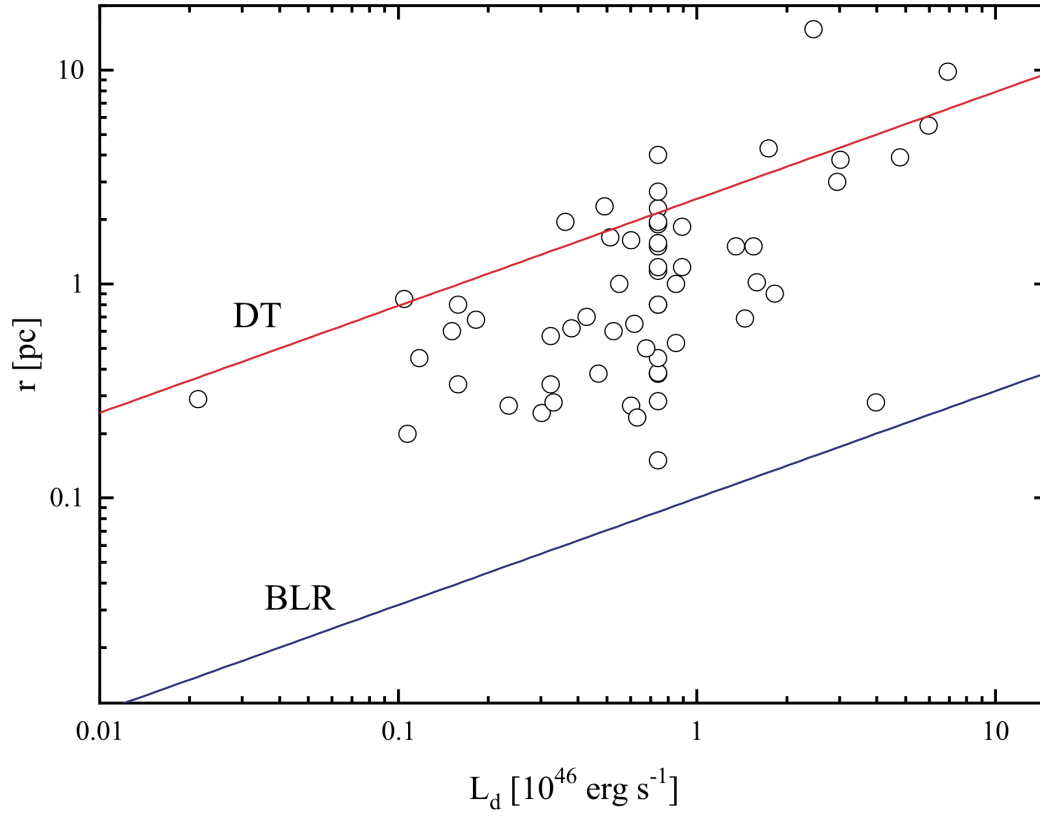


Figure 9. The location of the γ -ray emission region from the SMBH (x) as a function of the luminosity of an accretion disk (L_d). The sample sources are exhibited in open circles. The blue and red solid show the distances of BLR and DT, respectively.

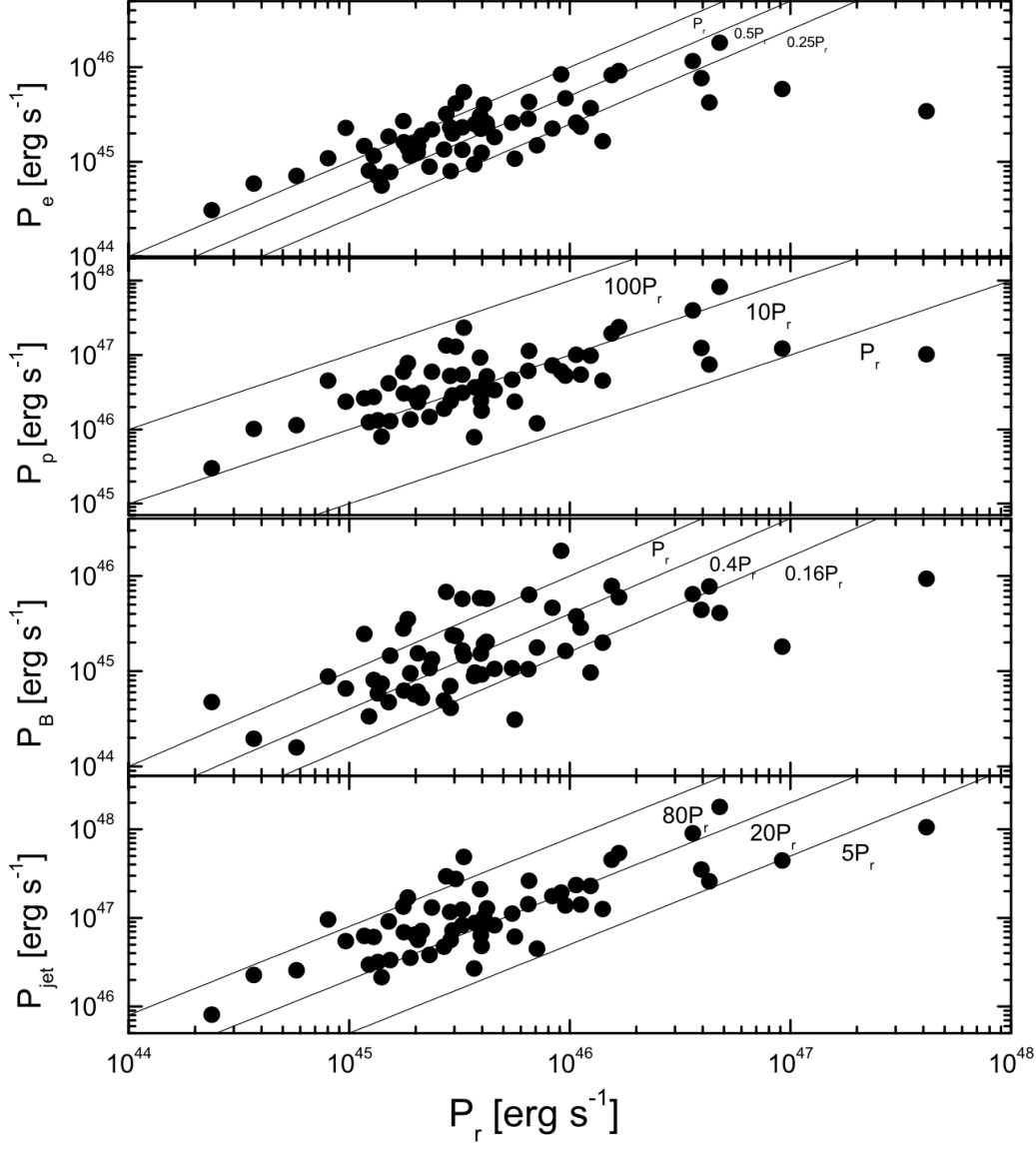


Figure 10. The P_e , P_p , P_B , P_{jet} as a function of the P_r .

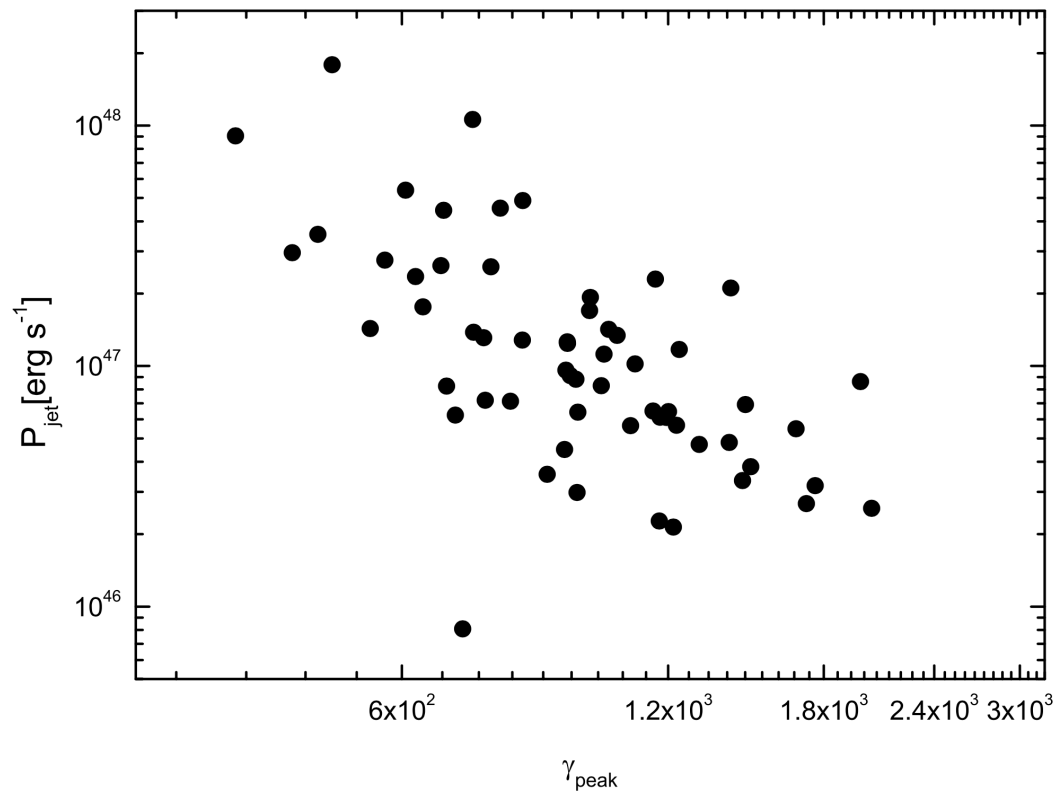


Figure 11. The P_{jet} as a function of the γ_{peak} .

Table 1
 Observation date between infrared to X-ray band, and the
 Integration date of γ rays for the FSRQs in our sample

Fermi Name (1)	Source Name (2)	RA(J2000) (3)	Dec(J2000) (4)	t_1^a (5)	t_2^b (6)
4FGL J0050.0-5736	PKS 0047-579	12.5197	-57.6164	2010/5/26-2010/6/1	2010/5/3-2010/7/3
4FGL J0051.1-0648	PKS 0048-071	12.7824	-6.8096	2009/5/17	2009/4/17-2009/6/17
4FGL J0109.7+6133	TXS 0106+612	17.445	61.5615	2010/1/31-2010/2/3	2010/1/1-2010/3/1
4FGL J0113.4+4948	S4 0110+49	18.3682	49.8054	2010/8/27	2010/7/27-2010/9/27
4FGL J0205.0-1700	PKS 0202-17	31.2637	-17.0022	2010/1/8	2009/12/8-2010/2/8
4FGL J0217.4+7352	S5 0212+73	34.3533	73.8804	2010/9/10-2010/9/11	2010/8/10-2010/10/10
4FGL J0217.8+0144	PKS 0215+015	34.4621	1.7346	2010/1/29-2010/2/2	2010/1/1-2010/3/1
4FGL J0221.1+3556	S4 0218+35	35.281	35.9359	2010/8/4	2010/7/4-2010/9/4
4FGL J0222.0-1616	PKS 0219-164	35.5197	-16.2787	2010/5/30	2010/4/30-2010/6/30
4FGL J0236.8-6136	PKS 0235-618	39.2021	-61.6106	2010/6/12-2010/6/16	2010/5/12-2010/7/12
4FGL J0407.5+0741	TXS 0404+075	61.8921	7.6998	2010/2/14-2010/2/15	2010/1/15-2010/3/15
4FGL J0438.4-1254	PKS 0436-129	69.6099	-12.9053	2010/7/1	2010/6/1-2010/8/1
4FGL J0457.0-2324	PKS 0454-234	74.2608	-23.4149	2010/2/24-2010/2/25	2010/1/25-2010/3/25
4FGL J0539.9-2839	PKS 0537-286	84.9952	-28.6585	2010/3/7-2010/3/12	2010/2/7-2010/4/7
4FGL J0601.1-7035	PKS 0601-70	90.2958	-70.5895	2010/3/9	2010/2/8-2010/4/8
4FGL J0654.4+4514	B3 0650+453	103.606	45.2446	2010/3/23	2010/2/23-2010/4/23
4FGL J0656.3-0322	TXS 0653-033	104.0765	-3.3686	2010/3/31	2010/3/1-2010/5/1
4FGL J0750.8+1229	OI 280	117.701	12.494	2010/4/5-2010/4/12	2010/3/8-2010/5/8
4FGL J0805.4+6147	TXS 0800+618	121.3557	61.7937	2010/4/3-2010/4/4	2010/3/4-2010/5/4
4FGL J0920.9+4441	S4 0917+44	140.2291	44.699	2009/10/29	2010/9/29-2010/11/29
4FGL J0956.7+2516	OK 290	149.1761	25.2817	2010/5/7-2010/5/15	2010/4/25-2010/6/25
4FGL J1037.7-2822	PKS B1035-281	159.4274	-28.3816	2010/1/22-2010/1/23	2009/12/22-2010/2/22
4FGL J1106.0+2813	MG2 J110606+2812	166.502	28.2254	2010/5/24	2010/4/24-2010/6/24
4FGL J1127.0-1857	PKS 1124-186	171.7634	-18.964	2010/6/10	2010/5/10-2010/7/10
4FGL J1147.0-3812	PKS 1144-379	176.76	-38.2006	2010/6/24	2010/5/24-2010/7/24
4FGL J1205.7-2635	PKS 1203-26	181.4322	-26.5946	2010/3/6-2010/3/7	2010/2/5-2010/4/5
4FGL J1208.9+5441	TXS 1206+549	182.2261	54.6995	2010/5/16-2010/5/21	2010/4/18-2010/6/18
4FGL J1222.5+0414	4C +04.42	185.6271	4.2389	2010/6/17	2010/5/23-2010/7/23
4FGL J1246.7-2548	PKS 1244-255	191.6887	-25.8018	2010/1/25	2009/12/25-2010/2/25
4FGL J1256.1-0547	3C 279	194.0415	-5.7887	2010/1/15	2009/12/15-2010/2/15
4FGL J1333.7+5056	CLASS J1333+5057	203.4395	50.9366	2010/3/13	2010/2/13-2010/4/13
4FGL J1347.6-3751	PMN J1347-3750	206.9135	-37.8633	2010/9/20	2010/8/20-2010/10/20
4FGL J1358.1+7642	S5 1357+76	209.5283	76.7064	2010/5/24-2010/5/25	2010/4/24-2010/6/24
4FGL J1408.9-0751	PKS B1406-076	212.2356	-7.8575	2010/5/23	2010/4/23-2010/6/23
4FGL J1436.9+2321	PKS B1434+235	219.2266	23.3611	2010/6/14	2010/5/14-2010/7/14
4FGL J1504.4+1029	PKS 1502+106	226.1033	10.4978	2010/7/29	2010/6/29-2010/8/29
4FGL J1514.8+4448	NVSS J151436+445003	228.7193	44.8105	2010/4/6	2010/3/6-2010/5/6
4FGL J1539.6+2743	MG2 J153938+2744	234.9019	27.7277	2010/3/17	2010/2/17-2010/4/17
4FGL J1549.5+0236	PKS 1546+027	237.3851	2.6084	2010/2/13-2010/2/20	2010/1/18-2010/3/18
4FGL J1635.2+3808	4C +38.41	248.8168	38.1401	2010/3/7	2010/2/7-2010/4/7
4FGL J1640.4+3945	NRAO 512	250.119	39.7626	2010/8/7	2010/7/7-2010/9/7
4FGL J1709.7+4318	B3 1708+433	257.4316	43.3109	2009/12/1	2009/11/1-2010/1/1
4FGL J1733.0-1305	PKS 1730-13	263.2632	-13.0858	2010/3/14	2010/2/26-2010/4/26
4FGL J1848.4+3217	B2 1846+32A	282.105	32.295	2010/10/6-2010/10/19	2010/9/7-2010/11/7
4FGL J1911.2-2006	PKS B1908-201	287.8078	-20.1137	2009/10/4	2009/9/4-2009/11/4
4FGL J1924.8-2914	PKS B1921-293	291.2136	-29.2468	2010/9/30	2010/8/30-2010/10/30
4FGL J1958.0-3845	PKS 1954-388	299.5026	-38.7547	2010/4/9-2010/4/14	2010/3/12-2010/5/12
4FGL J1959.1-4247	PMN J1959-4246	299.7963	-42.7852	2010/4/5-2010/4/14	2010/3/10-2010/5/10
4FGL J2135.3-5006	PMN J2135-5006	323.8362	-50.1015	2010/4/22-2010/5/5	2010/3/29-2010/5/29
4FGL J2145.0-3356	PMN J2145-3357	326.2533	-33.9439	2009/9/22-2009/9/24	2009/8/23-2009/10/23
4FGL J2151.8-3027	PKS 2149-306	327.9655	-30.46	2010/5-4-2010/5/13	2010/4/8-2010/6/8
4FGL J2157.5+3127	B2 2155+31	329.3862	31.4552	2009/7/8-2009/7/12	2009/7/10-2009/9/10
4FGL J2201.5-8339	PKS 2155-83	330.3787	-83.6631	2010/7/5-2010/7/17	2010/6/10-2010/8/10
4FGL J2212.0+2356	PKS 2209+236	333.0191	23.9334	2009/4/15-2009/4/21	2009/3/19-2009/5/19
4FGL J2225.7-0457	3C 446	336.4321	-4.9537	2010/5/22-2010/5/27	2010/4/24-2010/6/24
4FGL J2253.9+1609	3C 454.3	343.4963	16.1506	2009/12/4-2009/12/6	2009/11/5-2010/1/5
4FGL J2258.1-2759	PKS 2255-282	344.5288	-27.9843	2010/5/20-2010/5/26	2010/4/22-2010/6/22
4FGL J2321.9+3204	B2 2319+31	350.4779	32.0737	2009/5/20	2009/4/20-2009/6/20
4FGL J2327.5+0939	PKS 2325+093	351.8959	9.6543	2010/6/18-2010/6/21	2010/5/24-2010/7/24
4FGL J2334.2+0736	TXS 2331+073	353.5573	7.602	2009/12/20	2009/11/20-2010/1/20

^aThe simultaneous date from infrared to X-ray band.

^bThe integration time of the Fermi data.

Table 2
The Parameters Used to fit the SEDs

Fermi Name (1)	Source Name (2)	z (3)	$\log L_{\text{BLR}}$ (erg s $^{-1}$) (4)	R (10^{17} cm) (5)	B (G) (6)	δ (7)	s (8)	r (9)	N (10)	γ_0 (10^2) (11)	x (pc) (12)	χ^2 (13)
4FGL J0050.0-5736	PKS 0047-579	1.797	44.87 ^a	1.44	0.24	18	2.38	0.58	0.045	2.4	2.25	6.2
4FGL J0051.1-0648	PKS 0048-071	1.975	44.87 ^a	4	0.24	15	2.33	0.58	0.012	2	0.38	69.11
4FGL J0109.7+6133	TXS 0106+612	0.785	44.87 ^a	1	0.19	17	2.24	0.5	0.006	1.7	1.9	24.71
4FGL J0113.4+4948	S4 0110+49	0.389	44.87 ^a	1.2	0.18	9.5	1.79	0.6	0.049	2	1.15	1.59
4FGL J0205.0-1700	PKS 0202-17	1.74	44.87 ^a	2.35	0.24	9	1.95	0.61	0.121	1.6	0.38	8.96
4FGL J0217.4+7352	S5 0212+73	2.367	44.87 ^a	3.3	0.158	20	2.4	0.64	0.049	1.7	0.8	44.03
4FGL J0217.8+0144	PKS 0215+015	1.715	44.87 ^a	1.65	0.329	24	2.24	0.76	0.025	2.1	1.95	22.08
4FGL J0221.1+3556	S4 0218+35	0.944	44.87 ^a	1.9	0.147	15	1.85	0.77	0.013	3	4	31.41
4FGL J0222.0-1616	PKS 0219-164	0.698	44.87 ^a	1.6	0.18	10	2	0.65	0.041	2	0.284	7.52
4FGL J0236.8-6136	PKS 0235-618	0.465	44.87 ^a	0.55	0.49	11.1	1.98	0.83	0.18	2.3	0.384	38.29
4FGL J0407.5+0741	TXS 0404+075	1.133	44.51 ^b	1.7	0.209	15	2.05	0.9	0.032	2	0.34	15.19
4FGL J0438.4-1254	PKS 0436-129	1.276	44.78 ^b	2.65	0.22	12.5	2.05	0.58	0.029	1.4	0.27	10.81
4FGL J0457.0-2324	PKS 0454-234	1.003	44.87 ^a	2.81	0.364	12.11	2.18	0.62	0.009	2.2	0.8	12.11
4FGL J0539.9-2839	PKS 0537-286	3.104	44.87 ^a	4.95	0.115	23	2.28	0.87	0.017	1.5	1.5	24.95
4FGL J0601.1-7035	PKS 0601-70	2.409	44.69 ^b	2.3	0.242	22.49	2.1	0.53	0.01	2	2.3	15.68
4FGL J0654.4+4514	B3 0650+453	0.933	44.26 ^b	1.5	0.227	12	1.87	0.62	0.058	1.8	0.68	11.74
4FGL J0656.3-0322	TXS 0653-033	0.634	45.68 ^b	2.354	0.17	12.08	2.35	0.54	0.008	2.3	3.9	22.91
4FGL J0750.8+1229	OI 280	0.889	44.95 ^b	2.37	0.26	12.82	2.25	0.65	0.075	1.52	1.85	97.5
4FGL J0805.4+6147	TXS 0800+618	3.033	44.56 ^b	2.86	0.141	26.84	2	1.169	0.021	1.8	1.95	13.43
4FGL J0920.9+4441	S4 0917+44	2.19	45.775 ^b	2.6	0.278	20	2.2	0.68	0.03	2	5.5	51.93
4FGL J0956.7+2516	OK 290	0.708	44.93 ^b	1.48	0.245	10	1.78	0.75	0.062	2	0.53	19.08
4FGL J1037.7-2822	PKS B1035-281	1.066	44.95 ^b	1.41	0.23	14.34	1.89	0.58	0.06	1.32	1.2	4.5
4FGL J1106.0+2813	MG2 J110606+2812	0.844	45.16 ^b	2.03	0.22	10.9	1.78	0.835	0.008	3.2	0.69	7.22
4FGL J1127.0-1857	PKS 1124-186	1.048	44.87 ^a	2.9	0.238	10.7	2.001	0.631	0.01	3.2	2.7	73.83
4FGL J1147.0-3812	PKS 1144-379	1.048	44.48 ^b	2.4	0.303	13.78	2.35	0.66	0.021	2	0.25	12.53
4FGL J1205.7-2635	PKS 1203-26	0.789	44.07 ^b	1.84	0.143	15	2.02	0.59	0.005	2.6	0.45	6.42
4FGL J1208.9+5441	TXS 1206+549	1.345	44.52 ^b	1.6	0.31	10	1.78	0.72	0.048	2	0.28	7.19
4FGL J1222.5+0414	4C +04.42	0.966	44.97 ^c	2.1	0.21	11.5	1.73	0.853	0.063	1.7	0.57	5.22
4FGL J1246.7-2548	PKS 1244-255	0.635	44.87 ^a	1.07	0.188	18.6	2.05	0.881	0.041	2.3	1.2	21.99
4FGL J1256.1-0547	3C 279	0.536	44.78 ^b	3.05	0.34	13	2.35	0.68	0.033	1.5	1.6	353.3
4FGL J1333.7+5056	CLASS J1333+5057	1.362	44.37 ^b	1	0.29	15.32	2.1	0.74	0.011	3	0.27	2.44
4FGL J1347.6-3751	PMN J1347-3750	1.3	44.67 ^b	0.8	0.371	13.6	2.07	0.646	0.085	2.2	0.38	2.2
4FGL J1358.1+7642	S5 1357+76	1.585	44.2 ^b	1.2	0.18	20	2.08	0.63	0.029	2.3	0.8	2.5
4FGL J1408.9-0751	PKS B1406-076	1.494	45.47 ^b	1.55	0.293	17.6	1.85	0.98	0.034	1.93	3	46.22
4FGL J1436.9+2321	PKS B1434+235	1.544	44.72 ^b	2.26	0.16	19	1.9	1.24	0.004	3.3	0.6	11.98
4FGL J1504.4+1029	PKS 1502+106	1.839	45.24 ^b	2.2	0.204	16	2	0.96	0.014	3.32	4.3	46.94
4FGL J1514.8+4448	NVSS J151436+445003	0.57	43.33 ^b	0.9	0.22	18	1.57	1.31	0.015	2	0.29	8.77
4FGL J1539.6+2743	MG2 J153938+2744	2.19	44.63 ^b	1.36	0.197	20	2.1501	0.749	0.019	2.75	0.7	3.9
4FGL J1549.5+0236	PKS 1546+027	0.414	44.8 ^b	1.2	0.325	8.5	2.1	0.59	0.08	1.88	0.238	34.56
4FGL J1635.2+3808	4C +38.41	1.814	45.48 ^b	2.6	0.221	22	2.23	0.8	0.029	2	3.8	45.97
4FGL J1640.4+3945	NRAO 512	1.66	45.01 ^c	2	0.274	16	2.2	0.67	0.013	2.6	0.45	7.46
4FGL J1709.7+4318	B3 1708+433	1.027	44.03 ^b	1.28	0.3	14	2	0.66	0.016	2.6	0.2	3.2
4FGL J1733.0-1305	PKS 1730-13	0.902	44.83 ^b	2	0.278	20	2.2	0.7	0.019	1.7	0.5	89.23
4FGL J1848.4+3217	B2 1846+32A	0.798	44.58 ^b	0.79	0.3	15	2.31	0.702	0.055	3	0.62	59.06
4FGL J1911.2-2006	PKS B1908-201	1.119	44.87 ^a	2.55	0.32	15.2	2.08	0.75	0.016	2	1.55	18
4FGL J1924.8-2914	PKS B1921-293	0.352	44.02 ^b	3	0.27	10	2	0.93	0.021	2	0.85	42.37
4FGL J1958.0-3845	PKS 1954-388	0.63	44.2 ^b	1.51	0.235	11	1.91	0.7	0.057	2	0.34	34.11
4FGL J1959.1-4247	PMN J1959-4246	2.174	45.13 ^b	0.94	0.34	20	2	1	0.034	3	1.5	45.28
4FGL J2135.3-5006	PMN J2135-5006	2.181	45.26 ^b	1.2	0.21	21	2.1	1.02	0.053	2	0.9	2.97
4FGL J2145.0-3356	PMN J2145-3357	1.36	44.18 ^b	1.38	0.248	18.2	1.9	0.67	0.01	2.2	0.6	13.01
4FGL J2151.8-3027	PKS 2149-306	2.345	44.87 ^a	1.6	0.62	7	2.01	0.85	0.68	1.75	0.15	13.21
4FGL J2157.5+3127	B2 2155+31	1.488	44.74 ^b	1.14	0.28	18.75	2.18	0.72	0.048	2	1	7.36
4FGL J2201.5-8339	PKS 2155-83	1.865	45.19 ^b	1.3	0.3	17	2.07	0.7	0.048	2	1.5	12.03
4FGL J2212.0+2356	PKS 2209+236	1.125	44.79 ^b	1.2	0.28	15	1.8	1	0.035	2.2	0.65	6.33
4FGL J2225.7-0457	3C 446	1.404	45.6 ^b	3.62	0.335	13	2.22	0.7	0.015	2	0.28	33.79
4FGL J2253.9+1609	3C 454.3	0.859	45.39 ^b	3.1	0.28	25.5	2	1.285	0.0046	4	15.5	487.34
4FGL J2258.1-2759	PKS 2255-282	0.926	45.84 ^b	2.82	0.204	15	2.02	0.68	0.015	2	9.8	20.03
4FGL J2321.9+3204	B2 2319+31	1.489	44.71 ^b	1.85	0.204	17	1.85	0.73	0.015	2	1.65	31.59
4FGL J2327.5+0939	PKS 2325+093	1.843	45.2 ^b	3.01	0.219	10	1.6	1.159	0.077	1.8	1.02	14.48
4FGL J2334.2+0736	TXS 2331+073	0.401	44.93 ^b	1.05	0.29	7.5	1.9	0.72	0.095	2.02	1	74.81

^aThe average broad-line luminosity.

^bThe broad-line luminosity selected from [Xue et al. \(2016\)](#).

^cThe broad-line luminosity selected from [Ghisellini, & Tavecchio \(2009\)](#).

Table 3

The kinetic power in relativistic electrons, the power carried in magnetic field, the kinetic luminosity in cold protons, the radiative power, and the total jet power for FSRQs of our sample

Fermi Name (1)	Source Name (2)	P_e (erg s ⁻¹) (3)	P_B (erg s ⁻¹) (4)	P_p (erg s ⁻¹) (5)	P_r (erg s ⁻¹) (6)	P_{jet} (erg s ⁻¹) (7)
4FGL J0050.0-5736	PKS 0047-579	5.47E+45	1.45E+45	2.34E+47	3.30E+45	2.44E+47
4FGL J0051.1-0648	PKS 0048-071	4.25E+45	7.77E+45	7.47E+46	4.29E+46	1.30E+47
4FGL J0109.7+6133	TXS 0106+612	1.41E+45	3.52E+45	7.83E+46	1.84E+45	8.51E+46
4FGL J0113.4+4948	S4 0110+49	7.11E+44	1.58E+44	1.14E+46	5.76E+44	1.28E+46
4FGL J0205.0-1700	PKS 0202-17	3.69E+45	9.66E+44	9.81E+46	1.24E+46	1.15E+47
4FGL J0217.4+7352	S5 0212+73	1.82E+46	4.08E+45	8.26E+47	4.78E+46	8.96E+47
4FGL J0217.8+0144	PKS 0215+015	4.30E+45	6.36E+45	1.14E+47	6.53E+45	1.31E+47
4FGL J0221.1+3556	S4 0218+35	2.28E+45	6.58E+44	2.36E+46	9.65E+44	2.75E+46
4FGL J0222.0-1616	PKS 0219-164	1.08E+45	3.11E+44	2.36E+46	5.63E+45	3.07E+46
4FGL J0236.8-6136	PKS 0235-618	8.08E+44	3.35E+44	1.25E+46	1.23E+45	1.49E+46
4FGL J0407.5+0741	TXS 0404+075	1.82E+45	1.06E+45	3.38E+46	4.56E+45	4.12E+46
4FGL J0438.4-1254	PKS 0436-129	1.65E+45	1.99E+45	4.53E+46	1.41E+46	6.30E+46
4FGL J0457.0-2324	PKS 0454-234	1.34E+45	5.75E+45	3.11E+46	3.26E+45	4.14E+46
4FGL J0539.9-2839	PKS 0537-286	1.16E+46	6.42E+45	3.98E+47	3.61E+46	4.52E+47
4FGL J0601.1-7035	PKS 0601-70	3.07E+45	5.87E+45	9.27E+46	3.92E+45	3.92E+45
4FGL J0654.4+4514	B3 0650+453	1.62E+45	6.26E+44	3.06E+46	1.77E+45	3.46E+46
4FGL J0656.3-0322	TXS 0653-033	1.09E+45	8.76E+44	4.53E+46	8.01E+44	4.80E+46
4FGL J0750.8+1229	OI 280	4.16E+45	2.34E+45	1.29E+47	3.04E+45	1.38E+47
4FGL J0805.4+6147	TXS 0800+618	7.68E+45	4.39E+45	1.25E+47	3.95E+46	3.95E+46
4FGL J0920.9+4441	S4 0917+44	8.27E+45	7.83E+45	1.95E+47	1.55E+46	2.27E+47
4FGL J0956.7+2516	OK 290	1.35E+45	4.93E+44	1.90E+46	2.69E+45	2.36E+46
4FGL J1037.7-2822	PKS B1035-281	1.16E+45	8.10E+44	2.73E+46	1.29E+45	3.06E+46
4FGL J1106.0+2813	MG2 J110606+2812	9.41E+44	8.88E+44	7.87E+45	3.68E+45	1.34E+46
4FGL J1127.0-1857	PKS 1124-186	2.57E+45	2.04E+45	3.43E+46	4.19E+45	4.31E+46
4FGL J1147.0-3812	PKS 1144-379	2.61E+45	3.76E+45	1.01E+47	1.07E+46	1.18E+47
4FGL J1205.7-2635	PKS 1203-26	6.95E+44	5.84E+44	1.33E+46	1.35E+45	1.59E+46
4FGL J1208.9+5441	TXS 1206+549	1.25E+45	9.22E+44	1.79E+46	3.98E+45	2.41E+46
4FGL J1222.5+0414	4C +04.42	2.50E+45	9.64E+44	3.69E+46	3.71E+45	4.41E+46
4FGL J1246.7-2548	PKS 1244-255	1.90E+45	5.25E+44	3.11E+46	2.13E+45	3.57E+46
4FGL J1256.1-0547	3C 279	3.21E+45	6.81E+45	1.35E+47	2.75E+45	1.48E+47
4FGL J1333.7+5056	CLASS J1333+5057	5.62E+44	7.40E+44	8.02E+45	1.40E+45	1.07E+46
4FGL J1347.6-3751	PMN J1347-3750	1.26E+45	6.11E+44	2.86E+46	2.04E+45	3.25E+46
4FGL J1358.1+7642	S5 1357+76	2.32E+45	6.99E+44	5.24E+46	2.87E+45	5.83E+46
4FGL J1408.9-0751	PKS B1406-076	2.00E+45	2.39E+45	2.87E+46	2.94E+45	3.60E+46
4FGL J1436.9+2321	PKS B1434+235	1.50E+45	1.77E+45	1.21E+46	7.10E+45	2.25E+46
4FGL J1504.4+1029	PKS 1502+106	4.05E+45	1.93E+45	4.08E+46	4.08E+45	5.08E+46
4FGL J1514.8+4448	NVSS J151436+445003	3.09E+44	4.76E+44	3.02E+45	2.38E+44	4.05E+45
4FGL J1539.6+2743	MG2 J153938+2744	2.59E+45	1.08E+45	4.68E+46	5.47E+45	5.59E+46
4FGL J1549.5+0236	PKS 1546+027	8.01E+44	4.12E+44	2.42E+46	2.88E+45	2.83E+46
4FGL J1635.2+3808	4C +38.41	9.14E+45	5.99E+45	2.38E+47	1.67E+46	1.67E+47
4FGL J1640.4+3945	NRAO 512	2.36E+45	2.88E+45	5.46E+46	1.12E+46	7.10E+46
4FGL J1709.7+4318	B3 1708+433	8.87E+44	1.08E+45	1.48E+46	2.31E+45	1.91E+46
4FGL J1733.0-1305	PKS 1730-13	2.25E+45	4.63E+45	7.27E+46	8.33E+45	8.79E+46
4FGL J1848.4+3217	B2 1846+32A	1.86E+45	4.74E+44	4.18E+46	1.51E+45	4.57E+46
4FGL J1911.2-2006	PKS B1908-201	2.31E+45	5.76E+45	5.17E+46	4.21E+45	6.39E+46
4FGL J1924.8-2914	PKS B1921-293	1.47E+45	2.46E+45	2.62E+46	1.17E+45	3.13E+46
4FGL J1958.0-3845	PKS 1954-388	1.57E+45	5.71E+44	2.82E+46	1.98E+45	3.24E+46
4FGL J1959.1-4247	PMN J1959-4246	2.24E+45	1.53E+45	2.44E+46	3.95E+45	3.21E+46
4FGL J2135.3-5006	PMN J2135-5006	2.86E+45	1.05E+45	6.13E+46	6.48E+45	7.17E+46
4FGL J2145.0-3356	PMN J2145-3357	7.80E+44	1.45E+45	1.29E+46	1.53E+45	1.67E+46
4FGL J2151.8-3027	PKS 2149-306	5.88E+45	1.81E+45	1.23E+47	9.18E+46	2.22E+47
4FGL J2157.5+3127	B2 2155+31	2.20E+45	1.34E+45	5.97E+46	2.37E+45	6.56E+46
4FGL J2201.5-8339	PKS 2155-83	2.33E+45	1.65E+45	5.46E+46	3.26E+45	6.18E+46
4FGL J2212.0+2356	PKS 2209+236	1.16E+45	9.52E+44	1.37E+46	1.89E+45	1.77E+46
4FGL J2225.7-0457	3C 446	3.43E+45	9.31E+45	1.02E+47	4.14E+47	5.29E+47
4FGL J2253.9+1609	3C 454.3	8.41E+45	1.84E+46	6.04E+46	9.12E+45	9.63E+46
4FGL J2258.1-2759	PKS 2255-282	2.70E+45	2.79E+45	5.96E+46	1.76E+45	6.69E+46
4FGL J2321.9+3204	B2 2319+31	1.47E+45	1.54E+45	2.34E+46	2.05E+45	2.84E+46
4FGL J2327.5+0939	PKS 2325+093	4.71E+45	1.63E+45	5.31E+46	9.55E+45	6.90E+46
4FGL J2334.2+0736	TXS 2331+073	5.92E+44	1.95E+44	1.02E+46	3.69E+44	1.14E+46